International Journal of Solids and Structures 308 (2025) 113154

Contents lists available at ScienceDirect

International Journal of Solids and Structures

journal homepage: www.elsevier.com/locate/ijsolstr

Modeling viscoelasticity–viscoplasticity of high-strain composites for space deployable structures

Xiaowei Yue [a], Ruiwen Guo [a], Ning An [b,*], Jinxiong Zhou [a,*]

[a] State Key Laboratory for Strength and Vibration of Mechanical Structures, School of Aerospace, Xi'an Jiaotong University, Xi'an 710049, People's Republic of China

[b] Key Laboratory of Advanced Spatial Mechanism and Intelligent Spacecraft, Ministry of Education, School of Aeronautics and Astronautics, Sichuan University, Chengdu 610065, People's Republic of China

ARTICLE INFO

Dataset link: https://github.com/XJTU-Zhou-group/ABAQUS_UMAT_HSCcompVEVP

Keywords:
High-strain composites
Viscoelastic–viscoplastic
Anisotropic
Deployable structures
Permanent deformation

ABSTRACT

Space deployable structures made of thin-ply fiber-reinforced composite laminates exhibit significant time-dependent mechanical behaviors, including stress relaxation, shape recovery, and permanent residual deformation throughout their service period. Currently, there is a lack of an appropriate composite laminate model that is able to fully describe these phenomena. Here, we address this gap by proposing an anisotropic viscoelastic–viscoplastic continuum constitutive model to capture the mechanical behavior of composite deployable structures during folding, stowage, deployment, and recovery periods. The model adopts a viscoelastic formulation based on the Boltzmann integral, coupled with a Hill-type rate-dependent viscoplastic formulation. A detailed numerical implementation scheme using fully implicit integration with a two-step viscoelastic predictor and viscoplastic corrector strategy is provided. The accuracy and efficiency of the proposed model are validated against experimental results for both unidirectional and woven laminates. Simulations accurately capture the rate-dependent nonlinear stress–strain response, creep response under constant stress, and hysteresis loops in cyclic loading-unloading tests for single-ply lamina under various off-axis loading directions. Importantly, the proposed method is the first to capture the experimentally observed permanent deformation of real-world composite deployable structures, validated through column bending tests. This advanced modeling and simulation capability significantly enhances the simulation and design of space deployable structures.

1. Introduction

High-strain composites (HSCs) are extensively used in constructing large-scale spacecraft mechanisms that fit into small volumes for transport and then deploy in space. The applications include a variety of large apertures such as spaceborne communication antennas, imaging and sensing instruments, radar systems, solar power systems, solar sails, and other structures that transition from small launch configurations to much larger operational configurations (Murphey et al., 2015; Ma et al., 2024, 2022; Wang et al., 2023). These structures are typically made of thin-ply carbon fiber-reinforced laminates engineered to be foldable and deployable. Before launch, they are compactly folded to minimize space usage inside the rocket. The compact form will be maintained during the journey to orbit. Once the spacecraft reaches orbit, they are deployed to serve as supporting structures for constructing the aforementioned space mechanisms. To achieve higher packaging efficiency, the HSC-enabled deployable structures often experience high-strain deformation when being folded and stowed. Ultra-thin plies and specific structural designs, such as cut-outs and collapsible cross-sections of booms, are specially designed to prevent material failure when undergoing these high-strain deformations (Liu et al., 2024).

During the service life of composite deployable structures, they undergo several distinct deformation stages, each with different time scales ranging from seconds and minutes to months and even years. Understanding these stages and the associated rate (time-) dependent behaviors is essential for predicting and designing the performance of HSC deployable structures in space applications. These stages were originally summarized by Murphey et al. (2015). Here we present a detailed description of the service life of composite deployable structures, illustrated in Fig. 1, as follows:

(i) Fabrication: The composite laminates are fabricated to form the initial, intended shape, setting the baseline geometric configuration and mechanical properties of the deployable structure. According to the mechanics of composite materials, the effective properties of the laminates

* Corresponding authors.
E-mail addresses: anning@scu.edu.cn (N. An), jxzhouxx@mail.xjtu.edu.cn (J. Zhou).

https://doi.org/10.1016/j.ijsolstr.2024.113154
Received 11 September 2024; Received in revised form 29 October 2024; Accepted 20 November 2024
Available online 28 November 2024

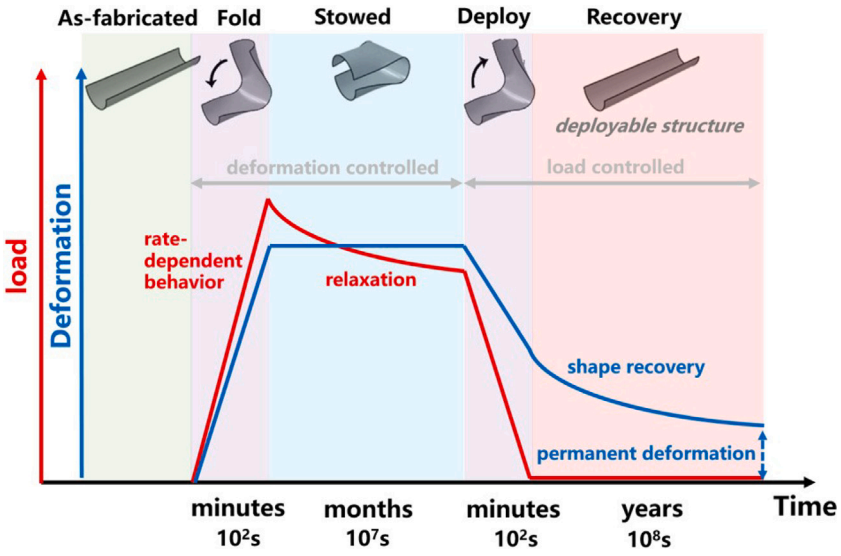

Fig. 1. Typical mechanical response of composite deployable structures during service life (this image is modified from Murphey et al. (2015)).

are anisotropic and can be determined by the properties of constituent fibers and polymers, as well as the micro and mesoscale arrangement of these materials. Fibers are typically considered purely elastic and transversely isotropic, while polymers exhibit isotropic, viscoelastic, and viscoplastic behaviors (Kim and Cho, 1992; Zhang et al., 2022). As a result, the composite laminate exhibits an anisotropic, viscoelastic, and viscoplastic behavior on a macroscopic scale.

(ii) Folding: The structure is folded into a compact state through a deformation-controlled loading process, with bending being the most commonly used deformation method. Although the folding process is typically slow (quasi-static), it may still exhibit rate-dependent behavior due to variations in loading rates, influenced by the viscous nature of the composites. During folding, strain energy is stored in the elastic deformation of the structure.

(iii) Stowage: Once folded, the structure is held in the compact state for an extended period, which may last from several days to months, depending on the duration of the spacecraft's journey to orbit. This prolonged constant deformation can result in significant stress relaxation due to the viscous nature of the composites, leading to a reduction in the stored strain energy (Kwok and Pellegrino, 2017; An et al., 2022). Additionally, plastic strains are also accumulated during this stowage period as the material yields (Yapa Hamillage et al., 2022; Ma et al., 2024; Guo et al., 2023).

(iv) Deployment: When the constraints holding the structure in its folded state are removed, the structure deploys. This deployment process can be either quasi-static, driven by external mechanisms in a slow and controlled manner, or transient dynamic, driven by the rapid release of stored strain energy, typically occurring quickly and dynamically (Deng et al., 2024; Firth and Pankow, 2020). During deployment, elastic deformation is recovered immediately, while viscous and plastic deformations are not.

(v) Recovery: After deployment, the structure enters a load-free state and undergoes a prolonged recovery period. During this recovery period, the viscous deformation of the structure gradually recovers, while the plastic deformation remains as permanent deformation (Guo et al., 2023).

Fig. 2 illustrates the concepts for modeling the structural behaviors of composite deployable structures throughout their complete service life. The most critical physical phenomena that need to be addressed include the rate-dependent folding and deployment behavior, stress relaxation and accumulation of plastic strains during stowage, and the time-dependent recoverable deformation and permanent plastic strains during and at the end of the recovery period. Table 1 summarizes the efficiency and shortcomings of various orthotropic constitutive models for laminates in terms of describing the mechanical behaviors of composite deployable structures. These models can be categorized into the following types: elastic (E), viscoelastic (VE), elastic–plastic (E–P), viscoelastic–plastic (VE–P), elastic–viscoplastic (E–VP), and viscoelastic–viscoplastic (VE–VP). E models can be used to capture the folding and deployment behavior and do not consider rate-dependent effects. VE models add time-dependence, making them suitable for rate-dependent folding and deployment, as well as stress relaxation during stowage and time-dependent recoverable deformation during recovery. P models add the capability to capture the permanent deformation generated at the fully folded state, which is also the permanent deformation at the end of the recovery period. VP models further add time-dependent plasticity, which reflects the increased accumulation of plastic deformation as stowage time increases in the stowage state.

Numerous efforts over the decades have been devoted to developing constitutive models to accurately simulate the behavior of deployable structures throughout different stages of their service life. In earlier works, the folding and deployment behaviors of these composite structures were primarily studied and described using purely elastic (E) laminate models. This approach was appropriate as the folding and deployment stages typically involve quasi-static loading conditions where the time-dependent effects of viscosity and plasticity were considered negligible. In this area, the fiber and matrix of composites are treated as purely elastic materials, and the effective elastic properties of lamina and laminates can be readily computed using micromechanics homogenization methods. Common approaches include Representative Volume Element (RVE) analysis (Goda et al., 2013; Omairey et al., 2019; Jin et al., 2024), Mechanics of Structural Genome (MSG) (Rouf et al., 2018; Yu, 2019; Liu et al., 2017), and FE^2 method (Ghosh et al., 1995; Feyel and Chaboche, 2000; Coenen et al., 2012). These lamina properties are then implemented to analyze the folding and deployment mechanics of composite deployable structures. Research has also been devoted to optimizing the design of the structures, such as cut-out optimization of tape-spring tubular hinges (Ferraro and Pellegrino, 2021; Jin et al., 2022; Liu et al., 2022) and cross-sectional shape optimization of thin-walled coilable booms (Bai et al., 2024; Jia et al., 2021).

Recently, researchers have realized that the stowage period before deployment significantly impacts the performance of deployable structures, especially when the stowage is prolonged and deployment is driven by the release of stored strain energy (Kwok and Pellegrino, 2013). This is because that, the stored strain energy, which drives the

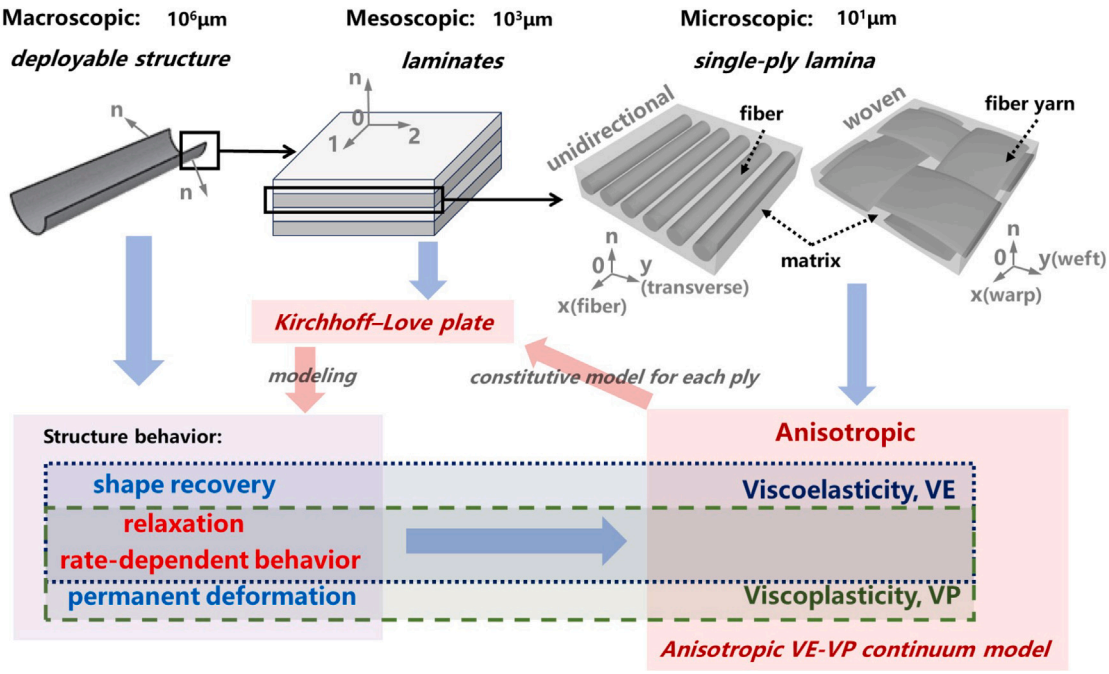

Fig. 2. Thin-ply modeling concept for describing the structural behaviors of composite deployable structures.

Table 1
Summary of anisotropic constitutive models for composite laminates.

Model	Folding & Deployment	Stowage		Recovery	
	Rate-dependent	Stress relaxation	Accumulation of plastic strains	Recoverable deformation	Irrecoverable deformation
E	NO	NO	NO	NO	NO
VE	YES	YES	NO	YES	NO
E–P	NO	NO	NO	NO	YES
VE–P	YES	YES	YES	YES	YES
E–VP	NO	NO	YES	NO	YES
VE–VP	YES	YES	YES	YES	YES

dynamic deployment of the structure, can be significantly reduced due to stress relaxation effects in the composites when the storage period is extended. In this situation, a viscoelastic (VE) constitutive model is necessary to accurately describe this stress relaxation phenomenon in laminates. To achieve this, multiscale modeling methods are employed to calculate the effective relaxation properties of lamina as function of stowage time, allowing for the simulation of the anisotropic viscoelastic behavior of composite structures. In these models, the fibers are assumed to be linear elastic materials, while the matrix is considered isotropic and linearly viscoelastic, described by a generalized Maxwell model using the Prony series (Kwok and Pellegrino, 2017). The effective relaxation modulus of the unidirectional lamina is calculated as a function of stowage time through microscale RVE analysis and then fitted into Prony series. These time-dependent lamina properties can be implemented in commercial finite element packages, such as ABAQUS, using built-in functions to define the layup of the laminates (Dassault, 2014), thereby simulating the macroscopic behavior of unidirectionally laminated shells. For woven composites, a second mesoscale homogenization is necessary to compute the stowage time-dependent ABD matrix for the laminates, which can be programmed into a user subroutine UGENS to simulate the macroscopic behavior of woven laminated shells (Liu et al., 2018; Hamillage et al., 2022; Rique et al., 2020). This multiscale method has been developed and applied by various research groups to simulate the stowage effect on the dynamic deployment performance of composite deployable structures, including tape-springs (Brinkmeyer et al., 2016; Borowski et al., 2018; Mao et al., 2017), tape-spring tubular hinges (Fernandes et al., 2021; An et al., 2022), thin-walled lenticular tube booms (Guo et al., 2023; Deng et al., 2024), and other configurations (Klimm and Kwok, 2020). Moreover, researchers have also attempted to use the VE models to simulate the recovery behavior of composite deployable structures (Long et al., 2022a; Hamillage et al., 2024). However, these models encountered difficulties in capturing residual permanent deformation because, for a VE material, the residual deformation always returns to the initial state if the recovery time is sufficient.

On the other hand, predicting the permanent deformation of composite deployable structures is crucial, as the recovery accuracy of the structure in the deployed configuration significantly impacts the performance of specific space deployable mechanisms such as communication antenna reflectors, imaging and sensing instruments, and radar systems. To achieve this, it is necessary to develop a viscoelastic–viscoplastic (VE–VP) constitutive model for the laminates, which accounts for the accumulation of plastic deformation during the stowage periods as well as permanent deformation after the long-term recovery period (Salazar and Fernandez, 2021; Ubamanyu et al., 2020; Yapa Hamillage et al., 2022). An intuitive method is to extend the micromechanics modeling method to calculate the anisotropic viscoelastic–viscoplastic properties of the laminate by performing RVE analysis, treating the fiber as a linear elastic material and the matrix as an isotropic viscoelastic–viscoplastic material (Long et al., 2022b; Chen et al., 2022). However, discretizing each micro and mesoscale architecture of the composite is impractical and often infeasible when simulating the macroscopic behavior of a deployable structure. It is urgent to develop a continuum anisotropic VE–VP model that directly represents the macroscopic

behavior of composite lamina. To the best of our knowledge, there remains a lack of such a model that can accurately reflect the entire service life of composite deployable structures. This paper aims to fill this research gap by developing a comprehensive anisotropic VE–VP continuum constitutive model for composite laminates.

Knowledge and advances in the field of composite mechanics provide the opportunity to develop such comprehensive continuum VE–VP models for anisotropic laminates. Relevant works on this topic may date back to the one-parameter flow rule for orthotropic plasticity proposed by Sun and Chen (1989), which captures the orthotropic elastic–plastic (E–P) behavior of unidirectional composites. Later, the model was extended by Sun and Gates (1990) to include elastic–viscoplastic (E–VP) behavior, enabling simulation of the time-dependent plastic behavior of orthotropic materials. Kawai and Masuko then carried out high-temperature constant-stress creep tests (Kawai and Masuko, 2004) and constant-strain relaxation tests (Masuko and Kawai, 2004) on plain coupon specimens of three types of angle-ply laminates, not only providing valuable experimental data but also validating the efficiency of the E–VP laminate model based on the basic concept proposed by Sun and Chen (1989). In addition, a similar modeling strategy has also been extended to describe the orthotropic elastic–plastic (E–P) behavior of woven composite laminates (Odegard et al., 2000; Ogihara and Reifsnider, 2002; Cho et al., 2010).

In the present work, an anisotropic VE–VP continuum model is developed and applied to both unidirectional and woven composites, aiming to enhance the accuracy of simulations for the mechanical behaviors encountered throughout the operational lifespan of composite deployable structures. The response of the composites comprises a combination of VE and VP components. The VE part employs a linear viscoelastic model expressed by Boltzmann's hereditary integral, capturing anisotropic behavior. The VP part uses a Hill-type equivalent stress to model the anisotropic yield behavior. A computational algorithm with fully implicit integration, utilizing a return mapping strategy based on a two-step VE predictor and VP corrector, is presented in detail. The anisotropic VE–VP model is then implemented into ABAQUS by developing a user-defined material subroutine (UMAT). A series of numerical simulations have been performed and compared with experimental tests to validate the accuracy and efficiency of the proposed model for modeling unidirectional (UD) and woven single-ply composites. The proposed method and ABAQUS UMAT are then applied to simulate the performance of a real-world deployable composite shell, using the "column bending tests" (CBT) designed and conducted by NASA and their collaborators for further validation. To the best of the authors' knowledge, among existing laminate models, our model is the first to fully capture both the relaxation effects and the residual permanent deformation of composite deployable structures.

The remaining content is organized as follows. Section 2 describes the formulation of the anisotropic VE–VP continuum model. Section 3 presents the computational algorithms used for finite element calculations. Section 4 presents the numerical cases matched with experimental results for validation and verification of the proposed model's accuracy and efficiency. Section 5 applies the method to analyze the folding, stowage, deployment, and recovery behaviors of a laminated composite shell, further validating the model's ability to describe the performance of a real-world composite deployable structure. Finally, Section 6 concludes the paper.

2. Viscoelastic–viscoplastic constitutive model formulation

The present model in this paper is based on an infinitesimal strain framework, where the total strain tensor $\boldsymbol{\varepsilon}$ of the composites is decomposed into a recoverable viscoelastic strain tensor $\boldsymbol{\varepsilon}^{ve}$ and an irrecoverable viscoplastic strain tensor $\boldsymbol{\varepsilon}^{vp}$:

$$\boldsymbol{\varepsilon} = \boldsymbol{\varepsilon}^{ve} + \boldsymbol{\varepsilon}^{vp} \tag{1}$$

This decomposition approach is widely used in modeling the nonlinear mechanical behavior of composites and has some physical basis (Miled et al., 2011; Jäger et al., 2015). Several studies have illustrated that the nonlinear stress–strain behavior of carbon fiber-reinforced polymer (CFRP) primarily results from the plastic deformation of the polymer (such as epoxy resin) matrix. The deformation mechanism of epoxy resin can be divided into two parts: deformation (viscoelasticity) and fracture rearrangement (viscoplasticity) of the molecular network chain Caruso et al. (2009), Nikolov et al. (2002).

2.1. Viscoelastic model

The relationship between the Cauchy stress tensor $\boldsymbol{\sigma}(t)$ and the history of the viscoelastic strain tensor $\boldsymbol{\varepsilon}^{ve}(s)$ for $s \leq t$ is described via a linear viscoelastic constitutive model based on the Boltzmann hereditary integral form:

$$\boldsymbol{\sigma}(t) = \int_0^t \boldsymbol{C}(t-s) : \frac{\partial \boldsymbol{\varepsilon}^{ve}(s)}{\partial s} ds \tag{2}$$

where $\boldsymbol{C}(t)$ is the fourth-order relaxation tensor, usually described in the form of the Prony series:

$$\boldsymbol{C}(t) = \boldsymbol{C}_\infty + \sum_{i=1}^{n} \boldsymbol{C}_i e^{-t/\rho_i} \tag{3}$$

where $\boldsymbol{C}_\infty$ is the long-term elastic modulus, $\boldsymbol{C}_i$ is the weight, and ρ_i is the relaxation time. The components in $\boldsymbol{C}(t)$ are usually fitted by the long-term relaxation test curves, and the mathematical form of Eq. (3) is sufficient to characterize the anisotropic viscoelasticity of the composites (Kwok and Pellegrino, 2017; Long et al., 2022a). There are also various methods for identifying viscoelastic parameters of composites based on RVE analysis and homogenization (An et al., 2022; Hamillage et al., 2022), which will not be discussed in this paper. Substituting Eq. (3) into Eq. (2) gives:

$$\boldsymbol{\sigma}(t) = \boldsymbol{C}_\infty : \boldsymbol{\varepsilon}^{ve}(t) + \sum_{i=1}^{n} \boldsymbol{C}_i : \boldsymbol{q}_i(t) \tag{4}$$

where:

$$\boldsymbol{q}_i(t) = \int_0^t e^{-(t-s)/\rho_i} \frac{\partial \boldsymbol{\varepsilon}^{ve}(s)}{\partial s} ds \tag{5}$$

2.2. Viscoplastic model

In the present work, viscoplastic strain tensor $\boldsymbol{\varepsilon}^{vp}$ characterizes the time-dependent irreversible deformation. The viscoplastic strain is defined by the plastic flow rule:

$$\dot{\boldsymbol{\varepsilon}}^{vp} = \dot{p} \frac{\partial f}{\partial \boldsymbol{\sigma}} = \dot{p} \boldsymbol{N} \tag{6}$$

where p is the equivalent plastic strain, which represents a kind of norm of the viscoplastic strain tensor. The function f is the plastic potential function, also referred to as the yield function in this study, due to the consideration of the associated flow rule. This function defines the shape of the yield surface and its evolution law during plastic flow. The term $\boldsymbol{N}$ in Eq. (6) represents the direction of plastic strain, and its mathematical form indicates that this direction is normal to the tangent plane of the yield surface. In the present study, the yield function is defined as follows:

$$f = f(\sigma_{eq}, r) = \sigma_{eq} - \left(r + r_0\right) \tag{7}$$

where σ_{eq} is the equivalent stress, representing a kind of norm of the stress tensor corresponding to the equivalent plastic strain. The equivalent stress is crucial as it characterizes the yield and plastic flow behavior of composites through its specific mathematical form, commonly referred to as the yield criterion.

Considering Hill's earlier related work (Hill, 1998), we can express the yield criterion with a general form as H:

$$2H(\sigma_{ij}) = a_{11}\sigma_x^2 + a_{22}\sigma_y^2 + a_{33}\sigma_z^2 + 2a_{12}\sigma_x\sigma_y + 2a_{13}\sigma_x\sigma_z + 2a_{23}\sigma_y\sigma_z + 2a_{44}\tau_{yz}^2 + 2a_{55}\tau_{xz}^2 + 2a_{66}\tau_{xy}^2 \tag{8}$$

where σ_{ij} is the component of the Cauchy stress tensor $\boldsymbol{\sigma}$, and a_{ij} is the anisotropy coefficient. Previous modeling of thin-ply composites has primarily based on the Kirchhoff–Love plate theory (Kwok and Pellegrino, 2017; Long et al., 2022a; Hamillage et al., 2024; Yu, 2024). Therefore, it is essential to define the constitutive relationship of the composite material based on the plane stress state. The plane stress form of Eq. (8) is:

$$2H(\sigma_{ij}) = a_{11}\sigma_x^2 + a_{22}\sigma_y^2 + 2a_{12}\sigma_x\sigma_y + 2a_{66}\tau_{xy}^2 \tag{9}$$

Several experiments have confirmed the anisotropic plastic flow behavior of both unidirectional and woven composite lamina. Specifically, unidirectional composites exhibit linear behavior in the fiber direction up until failure, while the nonlinearity is most significant in the transverse direction (Hahn and Tsai, 1973; Fallahi et al., 2020). Therefore, it is reasonable to make the following assumptions: Assumption 1: There is no plastic strain in the fiber direction of unidirectional composite lamina. Assumption 2: The stress component in the fiber direction of unidirectional composite lamina does not influence the yield function. The local coordinate system for unidirectional composites is illustrated in Fig. 2, where x represents the fiber direction and y represents the transverse direction. Based on Assumption 1:

$$\varepsilon_x^{vp} \equiv 0 \tag{10}$$

According to Assumption 2, in Eq. (9), $a_{11} = a_{12} = 0$, which can obtain:

$$2H(\sigma_{ij}) = \sigma_y^2 + 2a_{66}\tau_{xy}^2 \tag{11}$$

in which, without loss of generality, we further set $a_{22} = 1$. Let equivalent stress σ_{ij} defined as:

$$\sigma_{eq} = \sqrt{3H} \tag{12}$$

Substituting Eq. (11) into Eq. (12) gives:

$$\sigma_{eq} = \sqrt{\frac{3}{2}(\sigma_y^2 + 2a_{66}\tau_{xy}^2)} \tag{13}$$

The above equation represents the equivalent stress of unidirectional composites, a formulation first derived by Sun and Chen (Sun and Chen, 1989). In the Sun-Chen model, the yield surface and elastic domain are described as an infinitely extended elliptical cross-section cylinder in the plane stress space. The shapes of the yield surface and elastic domain on the $\sigma_x - \tau_{xy}$ and $\sigma_y - \tau_{xy}$ planes are illustrated in Figs. 3(a) and 3(b), respectively. Fig. 3(a) shows that the elastic domain extends infinitely in the fiber direction, indicating that stress in the fiber direction does not induce plastic flow in the composites, which aligns with Eq. (13). Additionally, Figs. 3(a) and 3(b) demonstrate that when unidirectional composites are loaded onto the yield surface along path-I or path-III, the plastic flow direction is $\boldsymbol{N}_1$, which is perpendicular to the tangent plane of the yield surface, as described in Eq. (6). Similarly, when the composites are loaded along path-II or path-IV, the plastic flow directions are $\boldsymbol{N}_2$ and $\boldsymbol{N}_3$, respectively. The nonlinearity of the woven composite lamina is minimal in the warp and weft directions but is most significant at a 45° orientation (Yang et al., 2018; Cho et al., 2010). Similar to unidirectional composites, it is reasonable to assume for woven composites that: Assumption 3: There is no plastic strain in the warp and weft direction in the woven composite lamina. Assumption 4: The stress component in the warp and weft direction of woven composite lamina does not affect the yield function. The local coordinate system of woven composites is shown in Fig. 2, where x is the warp direction and y is the weft direction. Based on Assumption 3:

$$\varepsilon_x^{vp} \equiv 0 \quad and \quad \varepsilon_y^{vp} \equiv 0 \tag{14}$$

According to Assumption 4, in Eq. (9), $a_{11} = a_{22} = a_{12} = 0$, which can obtain:

$$2H(\sigma_{ij}) = 2\tau_{xy}^2 \tag{15}$$

in which, without loss of generality, we further set $a_{66} = 1$. Substituting Eq. (15) into Eq. (12) gives:

$$\sigma_{eq} = \sqrt{\frac{3}{2}(2\tau_{xy}^2)} \tag{16}$$

The above equation describes the equivalent stress for woven composites. Similar results have been derived by Ogihara and Reifsnider (2002) and Odegard et al. (2000). The yield surface and elastic domain of the woven composite lamina are represented by the area between a pair of infinitely extended parallel planes in the plane stress space. The shapes of the yield surface and elastic domain on the $\sigma_x - \tau_{xy}$ and $\sigma_y - \tau_{xy}$ planes are shown in Fig. 3(c). Fig. 3(c) demonstrates that the elastic domain extends infinitely in the warp and weft directions, indicating that stress in these directions does not lead to plastic flow in the composites, which is consistent with Eq. (16). Additionally, Fig. 3(c) shows that when woven composites are loaded onto the yield surface along path-A or path-B, the plastic flow directions are $\boldsymbol{N}_1$ and $\boldsymbol{N}_2$, respectively. For the equivalent stress of woven composites presented in this paper, only two plastic flow directions are allowed in the shear component due to Assumptions 3 and 4. Despite the different yield and plastic flow behaviors characterized by the equivalent stress for unidirectional and woven composites, a general form can be provided:

$$\sigma_{eq} = \sqrt{\frac{3}{2}\boldsymbol{\sigma} : \boldsymbol{M} : \boldsymbol{\sigma}} \tag{17}$$

where $\boldsymbol{M}$ is the fourth-order tensor of the anisotropy coefficient. For unidirectional and woven composites, there are Voigt notation forms of $\boldsymbol{M}$ in plane stress space:

$$\boldsymbol{M} = \begin{pmatrix} 0 & 0 & 0 \\ 0 & 1 & 0 \\ 0 & 0 & 2a_{66} \end{pmatrix} \quad for\ unidirectional,$$
$$\boldsymbol{M} = \begin{pmatrix} 0 & 0 & 0 \\ 0 & 0 & 0 \\ 0 & 0 & 2 \end{pmatrix} \quad for\ woven \tag{18}$$

For simplicity, the present model has not considered the anisotropy in tension and compression for composites. Substituting Eq. (17) into Eq. (6), the thin-ply composites plastic flow rule can be given as:

$$\dot{\boldsymbol{\varepsilon}}^{vp} = \frac{3}{2}\dot{p}\frac{\boldsymbol{M} : \boldsymbol{\sigma}}{\sigma_{eq}} \tag{19}$$

In Eq. (7), r is an internal scalar variable used to describe the isotropic hardening behavior of the composites. The parameter r_0 characterizes the initial yield surface and can be treated as the initial value of r. Although internal variables in the form of second-order tensors can be defined to represent kinematic hardening behavior of composites, this approach is not considered in this paper. The evolution equation for the internal variable r is based on the superposition of two Voce nonlinear hardening laws (Voce, 1955), as follows:

$$\dot{r} = \sum_{i=1}^{2}\dot{r}_i = \sum_{i=1}^{2} b_i(Q_i - r_i)\dot{p} \tag{20}$$

where b_1, b_2, Q_1, and Q_2 are hardening parameters, which can be fitted from experimental curves. The nonlinear relationship between σ_{eq} and p shown as the rate-independent plasticity (red line) in Fig. 3(d) is governed by Eq. (20). The internal variable r is integrated over the loading history of the equivalent plastic strain p as follows:

$$r = \sum_{i=1}^{2} r_i = \sum_{i=1}^{2} r_i = Q_i(1 - e^{-b_i p}) \tag{21}$$

The Voce hardening law is characterized by an exponential equation, where the parameter Q_i determines the endpoint of the internal variable r's evolution. If Q_i is assigned a very small value, such that r

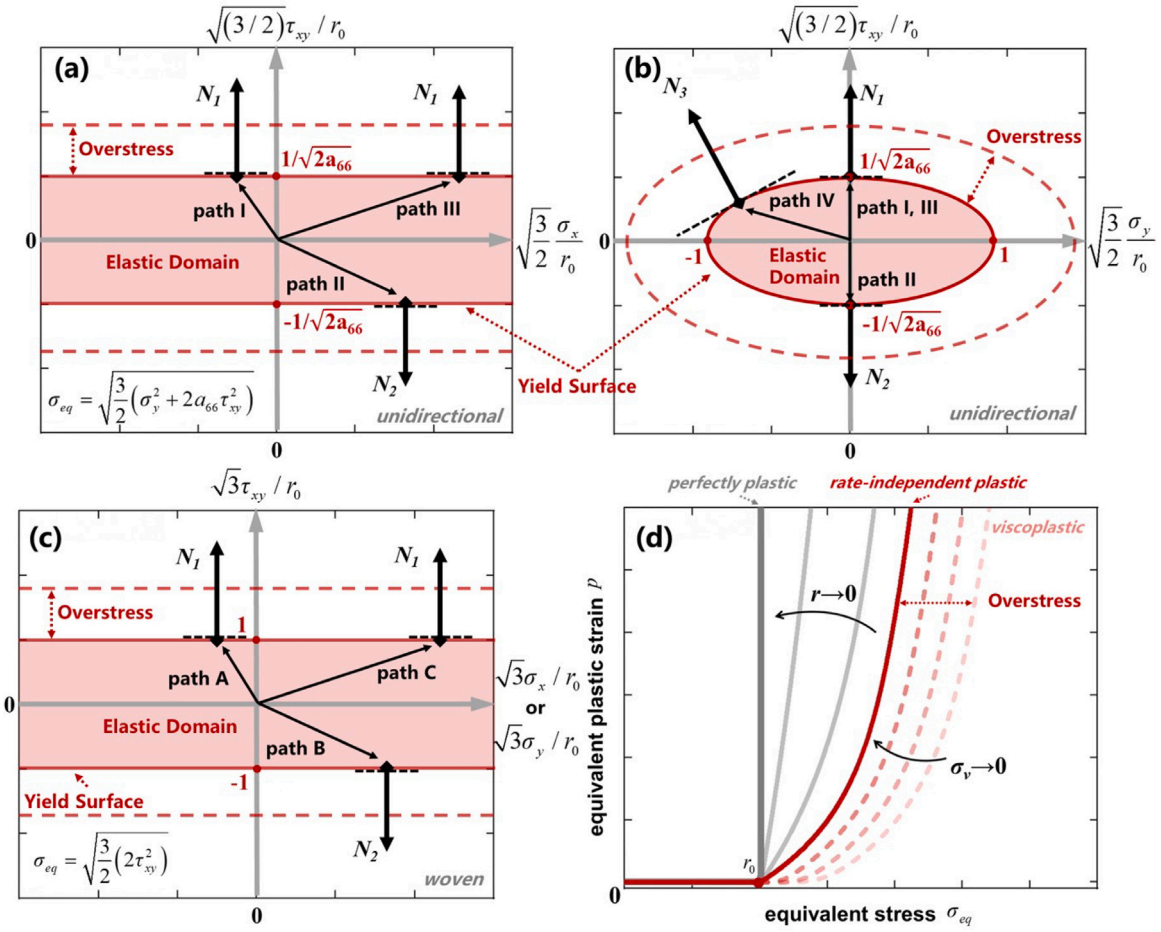

Fig. 3. Visualization of viscoplastic model: (**a**) yield surface and plastic flow direction in $\sigma_x - \tau_{xy}$ plane for unidirectional composites, (**b**) yield surface and plastic flow direction in $\sigma_y - \tau_{xy}$ plane for unidirectional composites, (**c**) yield surface and plastic flow direction in $\sigma_x - \tau_{xy}$ plane or $\sigma_y - \tau_{xy}$ plane for woven composites, (**d**) comparisons of perfect plasticity, rate-independent plasticity, and rate-dependent plasticity.

approaches zero, the rate-independent plastic model will reduce to a perfectly plastic model. Both the rate-independent plastic model with nonlinear hardening and the perfectly plastic model satisfied to the consistency condition:

$$f(\sigma_{eq}, r) \equiv 0 \tag{22}$$

The consistency condition is no longer satisfied for the viscoplastic model by introducing an overstress σ_v:

$$f(\sigma_{eq}, r) = \sigma_v \neq 0 \tag{23}$$

The phenomenological basis of the above equation is that, in a uniaxial tensile test controlled by strain, the stress response of the material increases with the strain rate (Chaboche, 2008). As the strain rate decreases, the stress–strain response of the material approaches that of a rate-independent plastic model, as illustrated in Fig. 3(d). The response beyond this rate-independent model is referred to as overstress in the viscoplastic model, as demonstrated in Figs. 3(a), 3(b), and 3(c). The overstress is determined by the viscosity equation in Norton form:

$$\sigma_v = K\dot{p}^m \tag{24}$$

where K and m are viscosity parameters, which can be fitted from experimental curves. Combining Eqs. (7), (23) and (24), it can be obtained the Perzyna-type viscoplastic function (Perzyna, 1966):

$$\dot{p} = \begin{cases} 0, & f \leq 0 \\ \varphi(\sigma_{eq}, p, r) = \left(\frac{\sigma_{eq} - (r + r_0)}{K}\right)^{1/m}, & f > 0 \end{cases} \tag{25}$$

3. Computational algorithm

In this section, we present the detailed numerical implementation algorithm for the proposed anisotropic viscoelastic–viscoplastic (VE–VP) model for thin-ply composites. The numerical implementation scheme discretizes the VE–VP model using the implicit backward Euler method. For the time interval $[t_n, t_{n+1}]$ defined by the time increment Δt, where the values of the variable at t_n and the total strain increment $\Delta\boldsymbol{\varepsilon}$ being known, the objective of the algorithm is to compute the values of the variable at time t_{n+1}. Define:

$$t_{n+1} - t_n = \Delta t \tag{26}$$

$$\boldsymbol{\varepsilon}(t_{n+1}) - \boldsymbol{\varepsilon}(t_n) = \Delta\boldsymbol{\varepsilon} \tag{27}$$

$$\boldsymbol{\varepsilon}^{ve}(t_{n+1}) - \boldsymbol{\varepsilon}^{ve}(t_n) = \Delta\boldsymbol{\varepsilon}^{ve} \tag{28}$$

$$\boldsymbol{\varepsilon}^{vp}(t_{n+1}) - \boldsymbol{\varepsilon}^{vp}(t_n) = \Delta\boldsymbol{\varepsilon}^{vp} \tag{29}$$

3.1. Incremental discretization scheme of viscoelastic model

The numerical solving scheme for the linear viscoelastic (VE) model is based on the approach originally proposed by Taylor et al. (1970). This method discretizes the Boltzmann hereditary integral into a recursive format that records the strain history via storing the state variables

at each time increment. According to Eqs. (4) and (5), the updated stress at time t_{n+1} is computed as follows:

$$\boldsymbol{\sigma}(t_{n+1}) = \boldsymbol{C}_\infty : \boldsymbol{\varepsilon}^{ve}(t_{n+1}) + \sum_{i=1}^{n} \boldsymbol{C}_i : \boldsymbol{q}_i(t_{n+1}) \tag{30}$$

where:

$$\boldsymbol{q}_i(t_{n+1}) = \int_0^{t_{n+1}} e^{-(t_{n+1}-s)/\rho_i} \frac{\partial \boldsymbol{\varepsilon}^{ve}(s)}{\partial s} ds \tag{31}$$

The integral term in Eq. (31) can be divided into two parts:

$$\boldsymbol{q}_i(t_{n+1}) = \int_0^{t_n} e^{-(t_{n+1}-s)/\rho_i} \frac{\partial \boldsymbol{\varepsilon}^{ve}(s)}{\partial s} ds + \int_{t_n}^{t_{n+1}} e^{-(t_{n+1}-s)/\rho_i} \frac{\partial \boldsymbol{\varepsilon}^{ve}(s)}{\partial s} ds \tag{32}$$

Substituting $\boldsymbol{q}_i(t_n)$ into the first term on the right side of Eq. (32), which can be given by:

$$\int_0^{t_n} e^{-(t_{n+1}-s)/\rho_i} \frac{\partial \boldsymbol{\varepsilon}^{ve}(s)}{\partial s} ds = e^{-\Delta t/\rho_i} \boldsymbol{q}_i(t_n) \tag{33}$$

The second term on the right side of Eq. (32) is the integral of the strain history $\boldsymbol{\varepsilon}^{ve}(s)$ over the time interval $[t_n, t_{n+1}]$. We suppose that the viscoelastic strain rate is constant over the time interval $[t_n, t_{n+1}]$, that is

$$\forall s \in [t_n, t_{n+1}] \quad \frac{\partial \boldsymbol{\varepsilon}^{ve}(s)}{\partial s} = constant \tag{34}$$

The above equations assume that the viscoelastic strain increases linearly within the time interval $[t_n, t_{n+1}]$ which is reasonable when Δt is small and has been adopted by several works like (Miled et al., 2011; Frank and Brockman, 2001; Ryou and Chung, 2009). Based on the Eq. (34), integration of the second term on the right side of Eq. (32) leads to:

$$\begin{aligned} \int_{t_n}^{t_{n+1}} e^{-(t_{n+1}-s)/\rho_i} \frac{\partial \boldsymbol{\varepsilon}^{ve}(s)}{\partial s} ds &= \frac{\Delta \boldsymbol{\varepsilon}^{ve}}{\Delta t} \int_{t_n}^{t_{n+1}} e^{-t_{n+1}/\rho_i} e^{s/\rho_i} ds \\ &= \frac{\rho_i}{\Delta t} \left(1 - e^{-\Delta t/\rho_i}\right) \Delta \boldsymbol{\varepsilon}^{ve} \end{aligned} \tag{35}$$

Combining Eqs. (32), (33) and (35) as follow:

$$\boldsymbol{q}_i(t_{n+1}) = e^{-\Delta t/\rho_i} \boldsymbol{q}_i(t_n) + \frac{\rho_i}{\Delta t} \left(1 - e^{-\Delta t/\rho_i}\right) \Delta \boldsymbol{\varepsilon}^{ve} \tag{36}$$

The above equation is the recursive form of Eq. (31), substituting Eq. (36) into Eq. (30) gives:

$$\boldsymbol{\sigma}(t_{n+1}) = \boldsymbol{C}_\infty : \boldsymbol{\varepsilon}^{ve}(t_{n+1}) + \sum_{i=1}^{n} \boldsymbol{C}_i : \left[e^{-\Delta t/\rho_i} \boldsymbol{q}_i(t_n) + \frac{\rho_i}{\Delta t} \left(1 - e^{-\Delta t/\rho_i}\right) \Delta \boldsymbol{\varepsilon}^{ve} \right] \tag{37}$$

The Eq. (37) represents the numerical format of the viscoelastic constitutive model as derived by Kwok and Pellegrino (2013), and is also referred to as the direct time integration (DI) approach by Noh and Whitcomb (2003). While Eq. (37) is sufficient for the numerical calculation of the purely viscoelastic (VE) model, the numerical implementation of coupling VE and VP models requires the full strain increment form of VE model due to the consideration of the return mapping algorithm. By comparing the expressions of Eq. (30) at times $t = t_{n+1}$ and $t = t_n$, it can be deduced that:

$$\boldsymbol{\sigma}(t_{n+1}) - \boldsymbol{\sigma}(t_n) = \boldsymbol{C}_\infty : \left(\boldsymbol{\varepsilon}^{ve}(t_{n+1}) - \boldsymbol{\varepsilon}^{ve}(t_n)\right) + \sum_{i=1}^{n} \boldsymbol{C}_i : \left(\boldsymbol{q}_i(t_{n+1}) - \boldsymbol{q}_i(t_n)\right) \tag{38}$$

Substituting Eq. (36) into Eq. (38) as follow:

$$\boldsymbol{\sigma}(t_{n+1}) = \boldsymbol{\sigma}(t_n) + \tilde{\boldsymbol{C}} : \Delta \boldsymbol{\varepsilon}^{ve} + \sum_{i=1}^{n} \left(e^{-\Delta t/\rho_i} - 1\right) \boldsymbol{C}_i : \boldsymbol{q}_i(t_n) \tag{39}$$

where:

$$\tilde{\boldsymbol{C}} = \boldsymbol{C}_\infty + \sum_{i=1}^{n} \boldsymbol{C}_i \frac{\rho_i}{\Delta t} \left(1 - e^{-\Delta t/\rho_i}\right) \tag{40}$$

Eq. (39) represents the stress-update algorithm for the viscoelastic (VE) part in the present VE–VP model. Here, $\tilde{\boldsymbol{C}}$ denotes the anisotropic incremental relaxation moduli described in Eq. (40), which also serves as the Jacobian matrix of the viscoelastic model in the form of Voigt notation, that is, $\partial \boldsymbol{\sigma} / \partial \boldsymbol{\varepsilon}^{ve} = \tilde{\boldsymbol{C}}$. By combining Eq. (39) with Eq. (30) and eliminating $\boldsymbol{\sigma}(t_n)$, the model degenerates to an isotropic case, obtaining a numerical implementation format consist with that presented by Miled et al. (2011).

3.2. Return mapping algorithm and implementation procedure

The return mapping algorithm for implementing the plastic model, originally developed by Simo and Taylor (1985), is used to determine the accurate stress state after a strain increment involved plastic. The fundamental approach involves evaluating the trial elastic stress for each strain increment, calculating the plastic component of the total strain increment, and subsequently correcting the trial stress to obtain the true stress state (Yue and Zhou, 2023). In the present anisotropic VE–VP models for thin-ply composites, the implementation follows a two-step approach: "viscoelastic predictor" and "viscoplastic corrector". The "viscoelastic predictor" scheme, as described by Eq. (39), proceeds as follows:

$$\boldsymbol{\sigma}^{pred}(t_{n+1}) = \boldsymbol{\sigma}(t_n) + \tilde{\boldsymbol{C}} : \Delta \boldsymbol{\varepsilon} + \sum_{i=1}^{n} \left(e^{-\Delta t/\rho_i} - 1\right) \boldsymbol{C}_i : \boldsymbol{q}_i(t_n) \tag{41}$$

If the predicted stress $\boldsymbol{\sigma}^{pred}(t_{n+1})$ satisfies $f\left(\boldsymbol{\sigma}^{pred}(t_{n+1})\right) \le 0$, then:

$$\boldsymbol{\sigma}(t_{n+1}) = \boldsymbol{\sigma}^{pred}(t_{n+1}) \tag{42}$$

Otherwise, the "viscoplastic corrector" step is required as follows:

$$\boldsymbol{\sigma}(t_{n+1}) = \boldsymbol{\sigma}^{pred}(t_{n+1}) - \tilde{\boldsymbol{C}} : \Delta \boldsymbol{\varepsilon}^{vp} \tag{43}$$

Eq. (43) provides a compact and general form for the return algorithm, which is independent of any specific VP model. It is form-identical to the E–VP model, except that incremental relaxation moduli replace the constant stiffness tensor. The isotropic form of Eq. (43) was proposed by Miled et al. (2011), and this work extends it to an anisotropic form suitable for modeling the mechanical response of composites. The key step in the "viscoplastic corrector" is solving for the plastic strain increment, which can be derived from the plastic flow rule Eq. (6):

$$\Delta \boldsymbol{\varepsilon}^{vp} = \Delta p \boldsymbol{N} \tag{44}$$

The form of $\boldsymbol{N}$ is determined by the equivalent stress, which has been discussed in Section 2.2. The algorithm for the equivalent plastic strain increment being required via discretizing the viscoplastic function Eq. (25) into incremental form as follows:

$$\dot{p} = \frac{\Delta p}{\Delta t} = \varphi(\sigma_{eq}, p, r) = \varphi(\sigma_{eq}^{pred}, \Delta p, p, r) \tag{45}$$

Let:

$$\psi(\sigma_{eq}, p, r) = \Delta p - \varphi(\sigma_{eq}, p, r)\Delta t = 0 \tag{46}$$

According to the hardening laws Eq. (20):

$$r(t_{n+1}) = r(t_n) + \Delta r \tag{47}$$

$$\Delta r = \sum_{i=1}^{2} \Delta r_i = \sum_{i=1}^{2} b_i (Q_i - r_i) \Delta p \tag{48}$$

Therefore, the nonlinear equation system Eqs. (45), (47) and (48) should be solved in the time interval $[t_n, t_{n+1}]$ via the Newton–Raphson method to obtain the equivalent plastic strain increment Δp. Considering the first-order Taylor expansion of Eq. (46):

$$\psi + \frac{\partial \psi}{\partial \Delta p} d\Delta p + \frac{\partial \psi}{\partial r} dr = 0 \tag{49}$$

Substituting Eq. (46) into Eq. (49) as follow:

$$\Delta p - \varphi \Delta t + \left(1 - \frac{\partial \varphi}{\partial \Delta p} \Delta t\right) d\Delta p - \frac{\partial \varphi}{\partial r} \Delta t dr = 0 \tag{50}$$

Table 2
Return mapping algorithm for the constitutive response in time interval $[t_n, t_{n+1}]$.

1. Obtain the history values at t_n: $\boldsymbol{\sigma}(t_n)$, $\boldsymbol{q}_i(t_n)$, $r(t_n)$, $p(t_n)$.
2. Evaluate $\boldsymbol{q}_i(t_{n+1})$ in $\Delta\boldsymbol{\epsilon}$ state via Eq. (36), compute $\bar{\boldsymbol{C}}$ via Eq. (40).
3. Compute $\boldsymbol{\sigma}^{pred}(t_{n+1})$ in $\Delta\boldsymbol{\epsilon}$ state via Eq. (41), prepare $f(\boldsymbol{\sigma}^{pred})$ via Eq. (7).
   IF $f < 0$ THEN go to 7. ENDIF.
4. Local Newton–Raphson: Prepare local RES and local Jacobian via Eqs. (51), (52) and (53), determine increments Δp, Δr.
   IF $RES < tol$ THEN go to 5. ENDIF.
5. Evaluate $\Delta\boldsymbol{\epsilon}^{vp}$ and $\Delta\boldsymbol{\epsilon}^{ve}$ via Eqs. (44) and (1)
6. Re-evaluate $\boldsymbol{q}_i(t_{n+1})$ in $\Delta\boldsymbol{\epsilon}^{ve}$ state via Eq. (36)
7. Compute $\boldsymbol{\sigma}(t_{n+1})$ via Eq. (42) or Eq. (43) and update state variable.

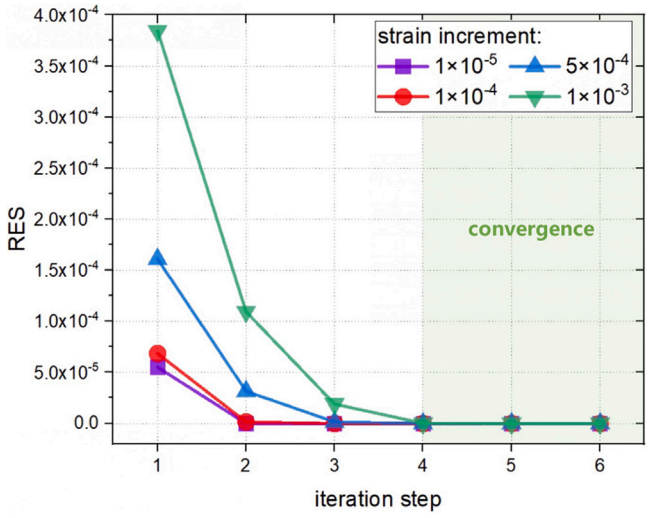

Fig. 4. Sufficient algorithm convergence for different strain increments.

In summary, the calculation method of Δp can be obtained based on the Newton–Raphson iterative scheme:

$$RES = \psi(\sigma_{eq}, p, r) = \Delta p - \varphi(\sigma_{eq}, p, r)\Delta t \tag{51}$$

$$d\Delta p = \frac{\varphi - \Delta p/\Delta t}{1/\Delta t - \partial\varphi/\partial\Delta p - \partial\varphi/\partial r\left(\Delta r_1 + \Delta r_2\right)} \tag{52}$$

$$\Delta p^{(k+1)} = \Delta p^{(k)} + d\Delta p \tag{53}$$

The computational implementation algorithm of the present VE–VP constitutive model is summarized in Table 2.

It should be noted that $\boldsymbol{q}_i(tn+1)$ must be recalculated using the viscoelastic strain increments over the time interval $[t_n, t_{n+1}]$ after obtaining the updated stress $\boldsymbol{\sigma}(t_{n+1})$ via the "viscoplastic corrector" procedure since the total strain increments were used in the prior calculation of $\boldsymbol{\sigma}^{pred}(t_{n+1})$. The numerical tangent stiffness of the VE–VP model, as shown in Eq. (40), is employed for the implicit finite element calculations. The computational implementation scheme proposed in the present work is adequately robust and converges within four iteration steps for fixed strain increments up to 1×10^{-3}, as illustrated in Fig. 4.

4. Verification and validation

The present model has been implemented using a user-defined material subroutine (UMAT) within the commercial finite element code ABAQUS. To validate the model's accuracy and efficiency, this section presents a series of benchmark simulations on the uniaxial tension behavior of single-ply lamina, including both unidirectional and woven lamina. The examples cover off-axis stress–strain behavior, rate-dependent behavior, creep behavior, and loading-unloading cyclic stress–strain behavior. Additionally, a numerical example is provided to demonstrate the model's efficiency in simulating the loading, holding, unloading, and recovery processes, which closely resemble the behavior of deployable structures.

Fig. 5(a) illustrates the geometry and dimensions of the single-ply lamina specimen used in this section. The local material directions and off-axis angle θ are defined for the unidirectional and woven laminates in Figs. 5(b) and 5(c), respectively. The constitutive behavior of the lamina is specified in the local material coordinate system, where the 1-direction aligns with the fiber direction for unidirectional lamina and the warp direction for woven lamina. Loading is applied along the x-axis in the global coordinate system, which corresponds to the longitudinal direction of the specimen. The angle between the 1-direction of the local material coordinates and the x-axis of the global coordinates is defined as the off-axis angle θ. In this section, the terms "axial stress" and "axial strain" refer to the stress and strain measured in the loading direction, as illustrated in Fig. 5.

In the FE simulations, the specimen was discretized using plane stress elements (CPS4 in ABAQUS). The nonlinear static general procedure was executed using the Abaqus/Standard solver. The left tab of the specimen was fixed, and uniaxial tension was applied to the right side. UMAT subroutines were developed to simulate the material behavior of the unidirectional lamina and the single-ply woven lamina, respectively. The unidirectional lamina was modeled using a viscoelastic–viscoplastic material framework, whereas the woven composite lamina was treated as an elastic–viscoplastic material. The material parameters were calibrated using experimental data sourced from Masuko and Kawai (2004), Kawai and Masuko (2004), Kawai and Taniguchi (2006). The instantaneous stiffness matrix for each lamina was determined by the engineering constants. The viscoelastic response is captured using a Prony series, with coefficients fitted from off-axis tension and relaxation test data. The viscoplastic component, on the other hand, was calibrated using equivalent stress-plastic strain curves obtained from off-axis tension tests. Further details regarding the calibration of lamina properties are provided in Appendix. Material properties are listed in Table A.1 for unidirectional lamina and Table A.2 for plain-weave woven lamina.

4.1. Off-axis stress–strain behavior of single-ply lamina

Finite element simulations for off-axis tensile tests of unidirectional and woven composite lamina were conducted to validate the modeling capability of the present constitutive model in capturing the anisotropic mechanical behavior of composites. In these simulations, tensile tests are conducted in displacement control mode, with a strain rate of 1%/min to align with experimental conditions. Fig. 6(a) presents the off-axis stress–strain responses for the unidirectional lamina across a range of off-axis angles from 0° to 90°. Note that the stress–strain curves for off-axis angles θ = 10°, 30°, and 45° were used to calibrate the model parameters as detailed in the Appendix, while those for θ = 0° and 90° served for validation. Additional simulation results at off-axis angles θ = 5°, 7°, 15°, and 20° further indicate that the proposed model can readily predict stress–strain responses for any off-axis angle. The simulation results show adequate agreement with the experimental observations. The results also demonstrate that the nonlinearity of the stress–strain response in unidirectional lamina strongly depends on the off-axis angle. At an off-axis angle of zero, where the lamina is loaded along the fiber direction, the stress–strain response remains linear, consistent with the assumption that stress in the fiber direction does not induce yielding and plastic flow, as described in Eq. (10). As the off-axis angle increases from 0° to 90°, the unidirectional lamina exhibits increasing nonlinearity in its stress–strain behavior. Fig. 6(b) presents the off-axis stress–strain responses for the single-ply woven lamina across a range of off-axis angles from 0° to 90°. Among these, the stress–strain curves for off-axis angles of θ = 15° and 30° were used to calibrate the model parameters, as detailed in Appendix. The stress–strain responses at off-axis angles of θ = 0°, 45°, and 90° were used for validation, and the simulation results showed satisfactory agreement

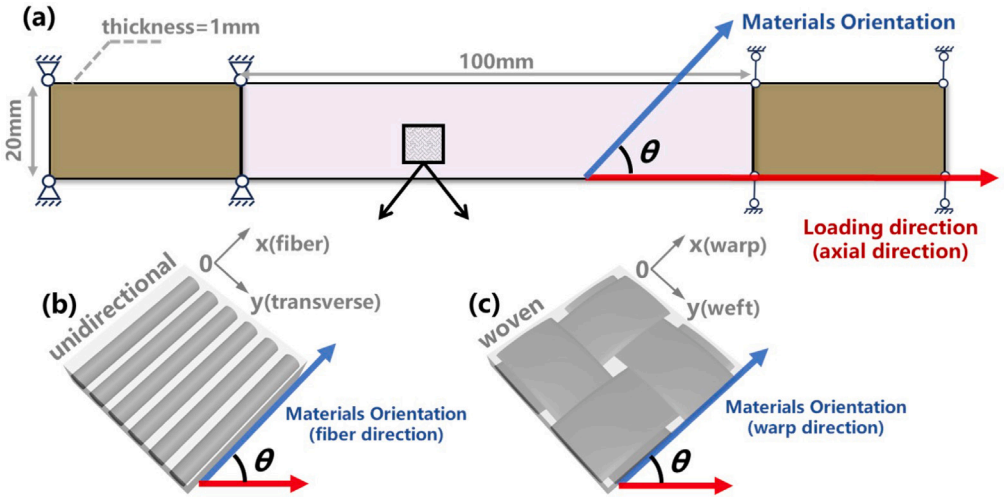

Fig. 5. Experimental scheme for off-axis mechanical behavior of single-ply lamina: (**a**) specimen geometry and materials orientation, (**b**) materials orientation for unidirectional composites, (**c**) materials orientation for woven composites.

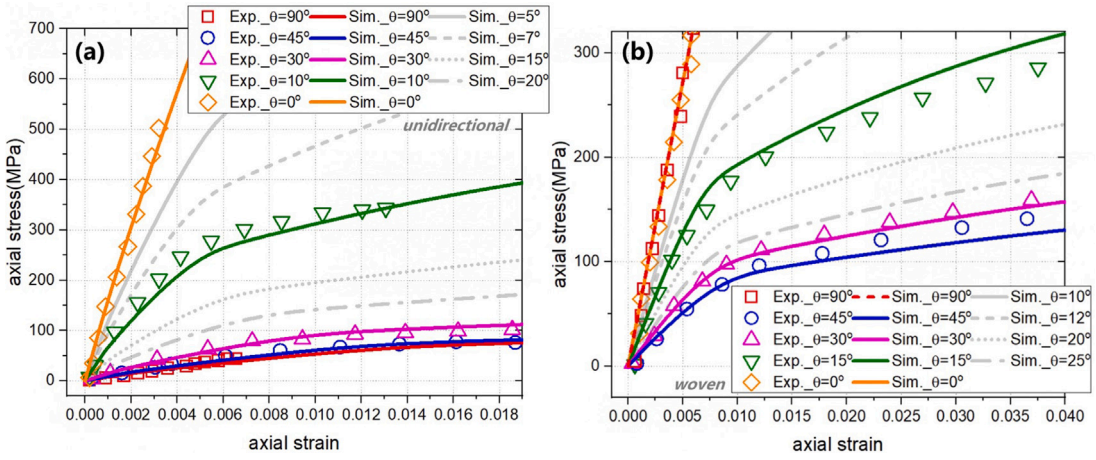

Fig. 6. Off-axis stress–strain curves: (**a**) single-ply unidirectional composites lamina, the experiment (Kawai and Masuko, 2004) are shown for comparison, (**b**) single-ply woven composites lamina, the experiment (Kawai and Taniguchi, 2006) are shown for comparison.

with the experimental data. Fig. 6(b) also provides results for off-axis angles of $\theta = 10°$, 12°, 20°, and 25°, indicating that the calibrated model can readily predict the stress–strain behavior of woven lamina at any arbitrary off-axis angle. The stress–strain response of the woven lamina is linear when the loading direction aligns with the warp and weft directions ($\theta = 0°$ and 90°), in accordance with the model's assumption that stress in these directions does not induce yield and plastic flow, as specified in Eq. (14). The woven lamina exhibits the most pronounced nonlinear stress–strain response at the 45° off-axis angle due to the axial stress induces maximum shear stress in the material orientation.

4.2. Off-axis time-dependent mechanical behavior of single-ply lamina

Finite element simulations of off-axis tensile tests for the unidirectional lamina were conducted at strain rates of 1%/min and 0.01%/min respectively, as illustrated in Fig. 7(a) and (b). Experimental data from Masuko and Kawai (2004) are also plotted in the same figure for comparison. The results indicate that, irrespective of the off-axis angles, the stress response at a given strain is higher at the faster strain rate. This rate-dependent stress–strain behavior of the composite lamina is accurately captured by the numerical simulations.

The uniaxial creep behaviors observed experimentally and predicted through simulations for unidirectional lamina with off-axis angles of $\theta = 30°$ and 45° are compared in Fig. 8(a) and 8(b), respectively. Experimental data from Kawai and Masuko (2004) are also plotted in the same figure for comparison. In the creep simulations, boundary conditions were stress-controlled. The creep stress was applied to the uniaxial creep model in a ramp mode over 20 seconds, after which the constant creep stress was maintained for 5 hours to evaluate the creep response of the composite lamina. As shown, a higher applied creep stress results in a larger axial creep strain response. The creep rate decreases with increasing creep time, eventually approaching a steady-state axial strain. The simulation predictions are in adequately agreement with the experimental observations.

4.3. Off-axis loading-unloading cycles behavior of single-ply lamina

Figs. 9(a) and 9(b) illustrate the cyclic loading-unloading responses of unidirectional composite lamina with fiber orientations of $\theta = 10°$ and 30°, respectively. The loading history is detailed in Table 3, with a loading and unloading strain rate of 1%/min. Experimental data from Kawai et al. (2020) are also plotted in the same figure for comparison. The experimentally observed loading-unloading stress–strain curves of the unidirectional lamina are shown as gray dash lines. Two main features can be summarized: **a.** Residual Axial Strain: After each unloading process, a residual axial strain is observed, which increases with the prior maximum axial tensile stress before unloading. This

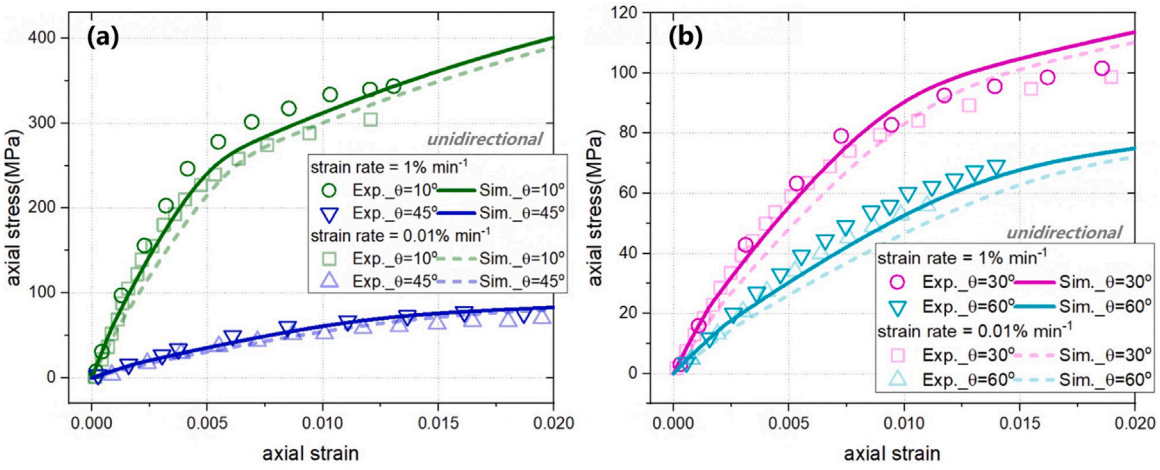

Fig. 7. Off-axis stress–strain curves of single-ply unidirectional composites lamina at different strain rates, the experiment (Masuko and Kawai, 2004) are shown for comparison: (**a**) $\theta = 10°$ and $\theta = 45°$, (**b**) $\theta = 30°$ and $\theta = 60°$.

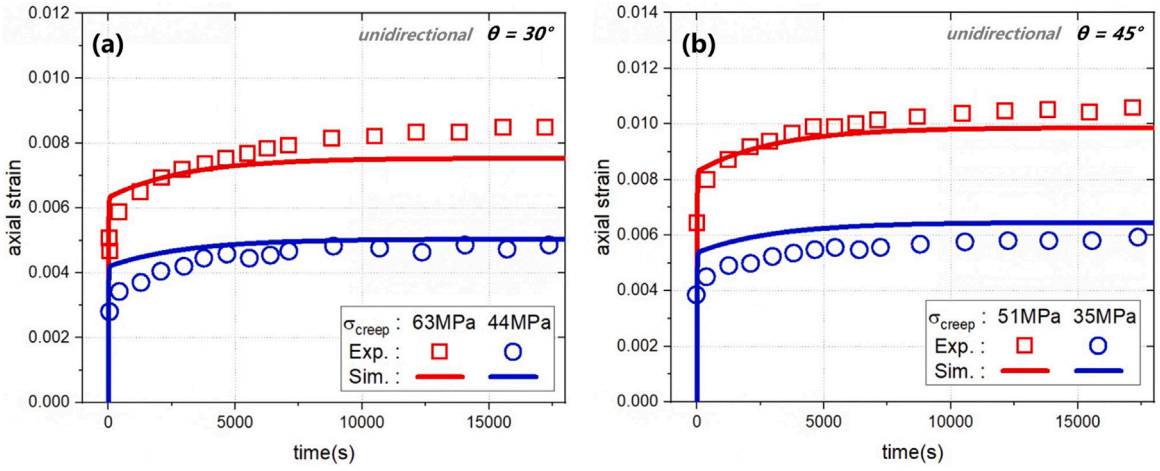

Fig. 8. Off-axis creep curves of single-ply unidirectional composites lamina, the experiment (Kawai and Masuko, 2004) are shown for comparison: (**a**) $\theta = 30°$, (**b**) $\theta = 45°$.

residual strain may consist of recoverable viscous strain, irrecoverable plastic strain, or a combination of both. **b.** Hysteresis Loop: The stress–strain curves during unloading and reloading do not overlap, forming a hysteresis loop. The width of this loop increases with the magnitude of the maximum axial tensile stress prior to unloading. For comparison, the simulation data predicted by an elastic–viscoplastic (E–VP) model proposed by Kawai and Masuko (2004), Masuko and Kawai (2004) are also plotted as blue lines in Figs. 9(a) and9(b). Although the E–VP model can capture the residual strain in the loading-unloading cycles, it fails to capture the hysteresis loop. This is because the stress state of the E–VP model remains within the elastic domain under unloading conditions ($f \leq 0$), and only when the stress state satisfies $f > 0$ does the E–VP model exhibit the time-dependent mechanical response governed by overstress σ_v (see Eq. (25)). The hysteresis loop observed in the loading-unloading cycles is attributed to creep recovery, where the residual deformation caused by the material viscosity during the loading process gradually recovers during the unloading process. Therefore, we conclude that extending the E–VP model to the VE–VP model is necessary to fully capture the time-dependent mechanical behavior of composites used in deployable structures.

4.4. Time-dependent mechanical response of constitutive models

Fig. 10 illustrates the time-dependent mechanical response of the constitutive model for a unidirectional composite lamina with a material orientation of 90°, where the simulation time step is shown in Table 4. The boundary conditions reproduce the typical loading history experienced by composite deployable structures during the service period, including folding, storage, deployment, and recovery. The material parameters used to calibrate the unidirectional lamina model are listed as detailed in Table A.1 in the Appendix, except make $K = 200$ MPa s^m in VE–VP and E–VP models for demonstration purposes. The mechanical responses of four time-dependent constitutive models: viscoelastic (VE), elastic–viscoplastic (E–VP), viscoelastic–viscoplastic (VE–VP), and viscoelastic–plastic (VE–P), under the same loading history, were compared. These four models are derived by degenerating

Table 3
History of loading-unloading cycles of UD lamina at a strain rate of 1%/min.

	Off-axial angle	Strain	Time increment (s)
Load1		0.003	18
Unload1		0.00065	14.1
Load2		0.0062	33.3
Unload2	$\theta = 10°$	0.0021	24.6
Load3		0.0095	44.4
Unload3		0.0045	30
Load4		0.015	63
Load1		0.0064	38.4
Unload1		0.0016	28.8
Load2	$\theta = 30°$	0.0128	67.2
Unload2		0.00510	46.2
Load3		0.02	89.4

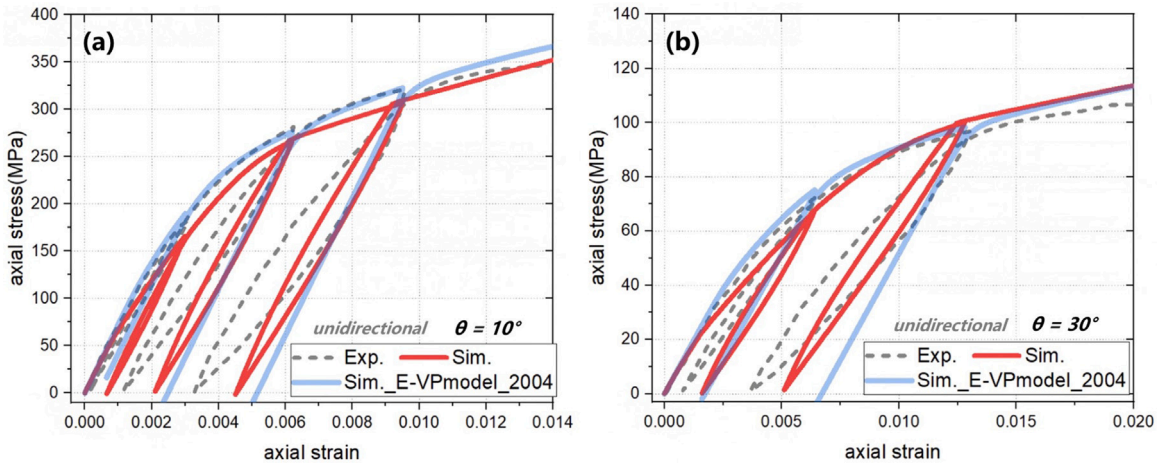

Fig. 9. Off-axis loading-unloading stress–strain cycles response of single-ply unidirectional composites lamina, the experiment (Kawai et al., 2020, gray dash line) and previous simulation based on elastic–viscoplastic (E–VP) model by Kawai (Kawai and Masuko, 2004, blue line) are shown for comparison: (**a**) $\theta = 10°$, (**b**) $\theta = 30°$.

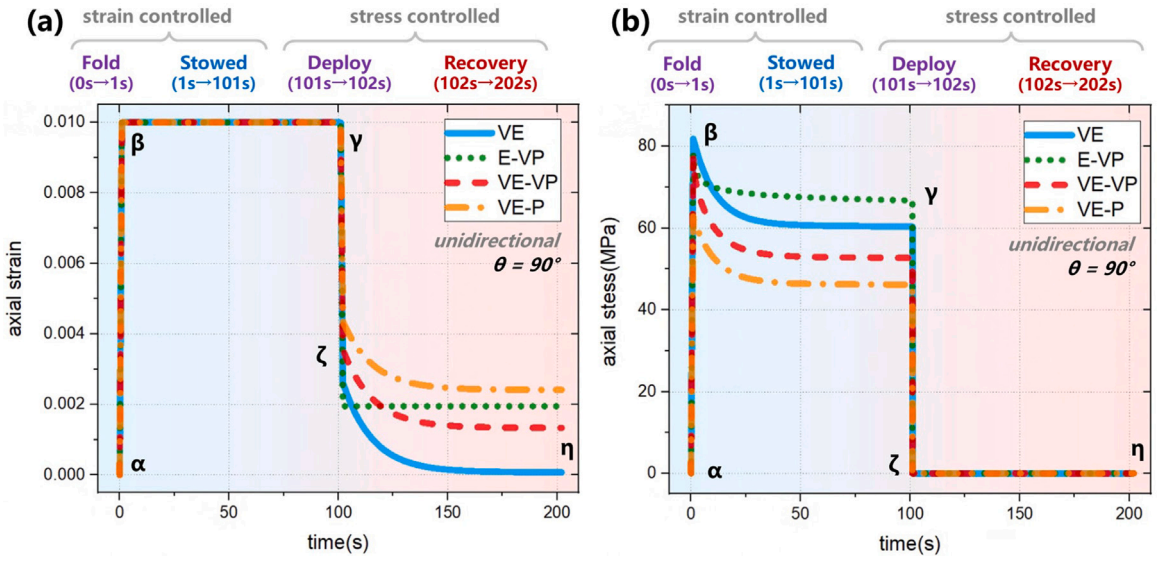

Fig. 10. Relaxation and recovery response of single-ply unidirectional composites lamina based on viscoelastic–viscoplastic (VE–VP) model, the viscoelastic (VE) model, elastic–viscoplastic (E–VP) model and viscoelastic–plastic (VE–P) model responses are shown for comparison: (**a**) strain–time curves, (**b**) stress–time curves.

Table 4
Typical loading history of composites in service period.

Step period	fold($\alpha \to \beta$)	stowed($\beta \to \gamma$)	deploy($\gamma \to \zeta$)	recovery($\zeta \to \eta$)
Step times t (s)	1	100	1	100

the viscoelastic–viscoplastic (VE–VP) constitutive model described in Section 2. Specifically, the VE–VP model reduces to the VE model when the initial yield surface parameter r_0 is set to infinity, ensuring that the model remains within the viscoelastic domain throughout loading. The VE–VP model degenerates into the E–VP model when the relaxation time ρ_i in the VE–VP model is infinite, and the relaxation moduli tensor degenerates to the constant stiffness tensor via setting $\boldsymbol{C}_i$ to zero and $\boldsymbol{C} = \boldsymbol{C}_0 = \boldsymbol{C}_\infty$ in the implementation. The VE–VP model can degenerate into the VE–P model when the yield function f satisfies the consistency condition outlined in Eq. (22) via the parameter K in the viscosity equation Eq. (24) is set to a sufficiently small value, such as 1, ensuring that the overstress σ_v can be neglected.

The axial stress–time curve in Fig. 10(b) illustrates the stress relaxation response of the composite lamina during the storage period ($\beta \to \gamma$). Despite different underlying mechanisms, all models demonstrate the ability to capture the stress relaxation behavior of composites. The stress relaxation in the VE and VE–P models arises from the time-dependent decrease of the relaxation moduli tensor $\boldsymbol{C}(t)$ as described by Eq. (3). In contrast, the stress relaxation in the E–VP model is attributed to the viscosity equation Eq. (24): under constant strain over a prolonged period, the overstress σ_v decreases, and the stress state returns to the yield surface along the direction of $\boldsymbol{N}$ over time. The VE–VP model combines both of these mechanisms. Fig. 10(a) compares the time-dependent mechanical responses of the composite constitutive models during the deployment and recovery periods. The VE model, commonly used to simulate the time-dependent mechanical behavior of composite deployable structures, effectively captures the lamina's recovery behavior. When the constraint on the material is removed, and the axial stress drops to zero during the deployment period ($\gamma \to \zeta$), the instantaneous elastic strain is eliminated, leaving a residual axial strain at point ζ, which gradually decreases to zero over time during the recovery period ($\zeta \to \eta$). This indicates that the residual axial strain at point ζ is fully recoverable for the VE model. For the E–VP model, the axial strain remains constant at a non-zero value during the recovery period ($\zeta \to \eta$), implying that the residual axial strain at point ζ is entirely irrecoverable. In contrast, for the VE–VP and VE–P models,

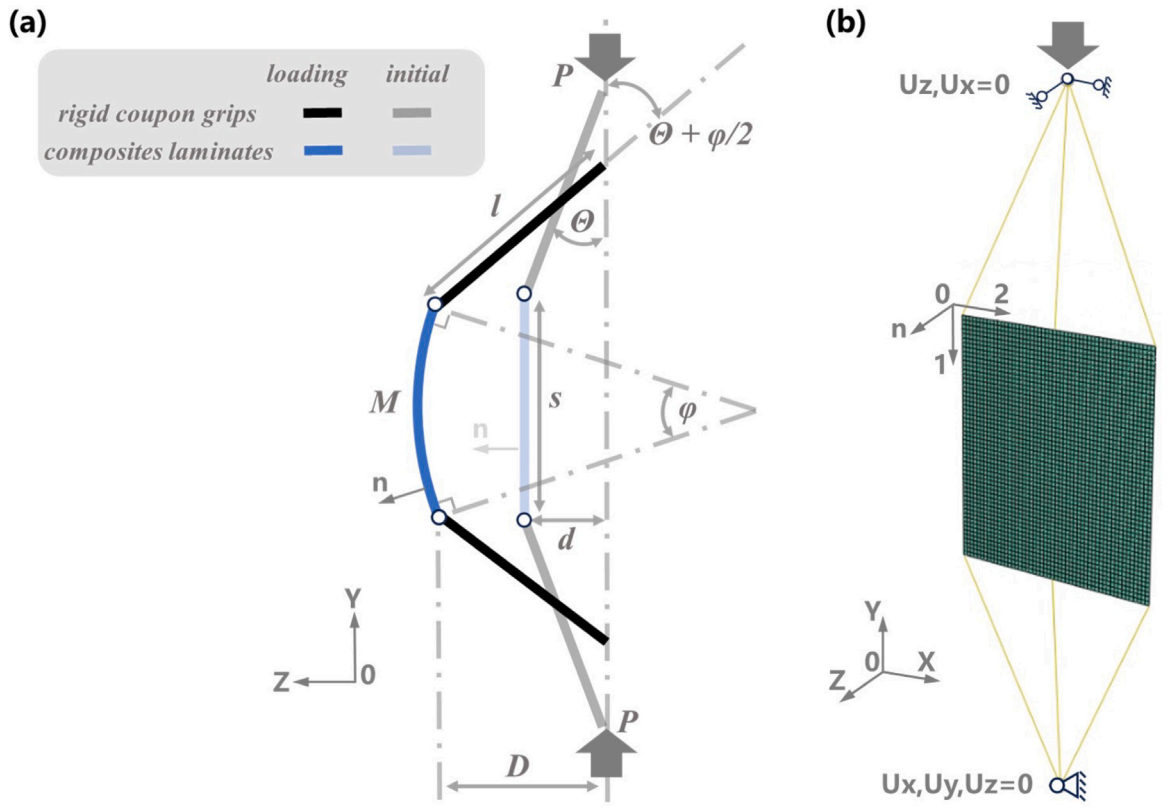

Fig. 11. Schematic of the column bending test (CBT) and FEM model (Salazar and Fernandez, 2021; Long et al., 2022a): (**a**) initial configuration and deformed configuration, (**b**) geometry and boundary conditions.

the residual axial strain at point ζ gradually decreases over time but approaches a non-zero value during the recovery period ($\zeta \to \eta$). This suggests that the residual axial strain at point ζ for both the VE–VP and VE–P models has recoverable and irrecoverable components, offering a more comprehensive description of the time-dependent mechanical behavior of composite laminae in deployable structures throughout their service life.

5. Simulation of the column bending test

The composite deployable structure undergoes significant volume reduction through large bending deformations during its service life. Fernandez and Murphey (2018) developed the Column Bending Test (CBT) as a method to characterize the bending behavior of thin-ply composite laminates, specifically designed for high-strain composites. This test not only be used to validate but also calibrate the mechanical models of thin-ply composites. The CBT experimental setup minimizes direct contact between the composite laminate and the loading indenter, thereby addressing the limitations of traditional bending test methods, such as four-point bending (Salazar and Fernandez, 2021). By implementing a compression state in the specimen, the CBT generates a stress state that closely approximates pure bending in the composite laminate. Numerical simulations of the CBT provide a valuable tool for evaluating the present composite constitutive model and offer deeper insights into the experimental observations obtained through CBT.

5.1. Experimental and modeling procedure

The CBT experimental setup is depicted in Fig. 11(a). In this setup, the composite laminate is secured within the testing apparatus using a pair of rigid grips, allowing the ends of the gauge length s to rotate freely. Initially, the normal vector $\boldsymbol{n}$ of the composite laminate is oriented perpendicular to the loading axis, with the angle θ between the rigid grips and the loading axis. The specimen is subjected to compressive loading from the initial configuration to the deformed configuration under displacement control, offsetting the laminate from its initial position to a state approximating pure bending. The directly measured quantities in the CBT are the reaction force P and the displacement δ of the test fixture, and the corresponding moment M and the angle change φ of the composite laminate can be derived via mathematical conversions based on geometric relationships, as detailed in Fernandez and Murphey (2018). NASA conducted CBT experiments on woven composite laminates, and reproduced the service life conditions of composite deployable structures, including the fold, stowed, deploy, and recovery periods (Salazar and Fernandez, 2021). In the folding step, the specimen was bent to a curvature representative of real-world service conditions. In the storage step, this curvature was maintained constant extending to six hours (21600 seconds). In the deployment step, the specimen was returned to a load-free state, and in the final recovery step, where it remained in a load-free state for an additional 10000 seconds. The specific loading history is detailed in Table 5.

Table 5
Loading history of the CBT.

Step period	fold	stowed	deploy	recovery
Step times t (s)	120	21,600	120	10 000

The finite element simulation of the CBT experiment was conducted using ABAQUS CAE, with the geometry, boundary conditions, and loading history consistent with the experimental setup, as depicted in Fig. 11(b). The composite laminate model was discretized into 2805 fully integrated four-node shell elements (S4 in ABAQUS). The rigid grips of the specimen were modeled through interaction contact between reference points and the edges of the composite laminate, with further modeling details provided in Long et al. (2022a). The key

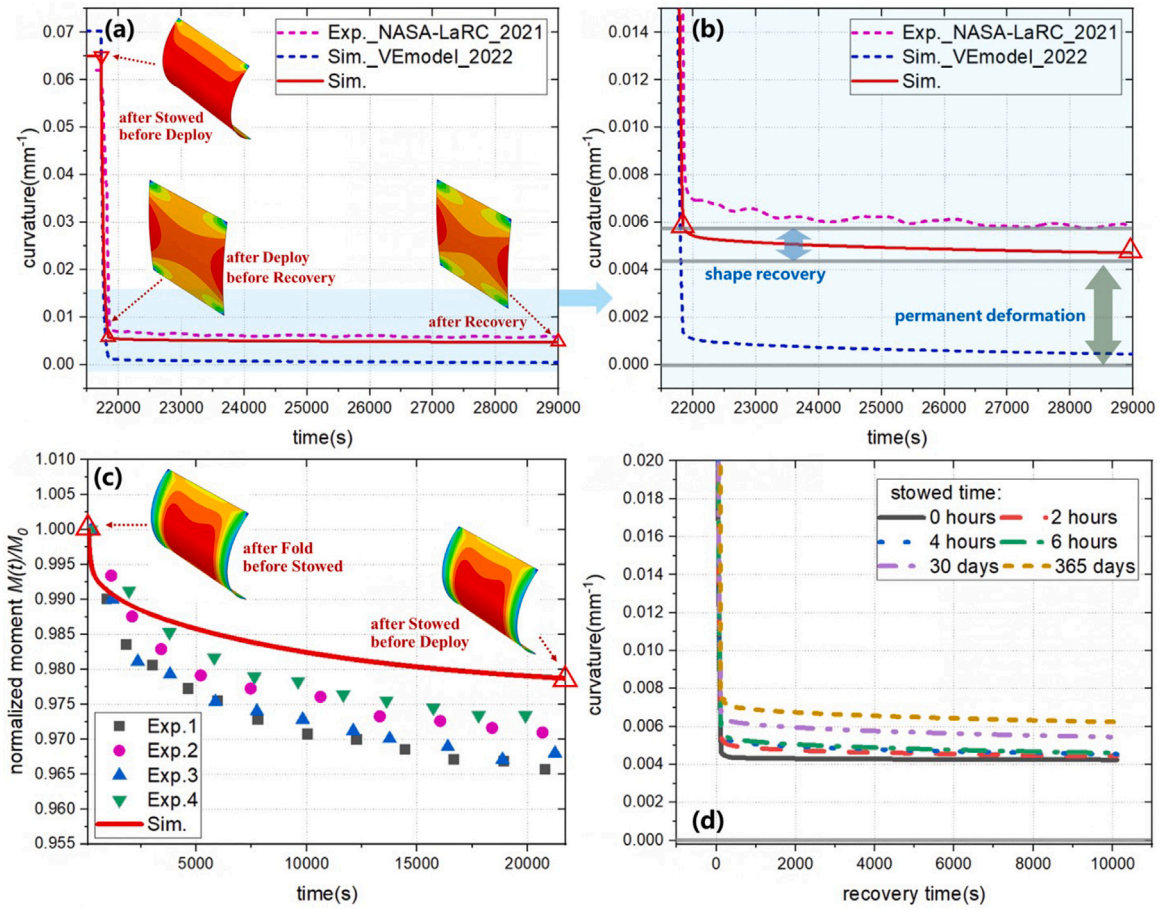

Fig. 12. History of laminates mechanical responses during fold, stowed, deploy and recovery: (**a**) curvature-time curves of laminates during recovery (red line), the experiment by NASA (Salazar and Fernandez, 2021, purple dash line) and previous simulation based on viscoelastic (VE) model by Yu (Long et al., 2022a, blue dash line) are shown for comparison, curvature distribution of laminates at different times are shown, (**b**) detailed curvature-time curves of laminates during recovery, (**c**) normalized moment relaxation curves during stowed (red line), the experiment by NASA (Salazar and Fernandez, 2021, dot) are shown for comparison, section moment distribution of laminates at different times are shown, (**d**) curvature-recovery time curves of laminates during recovery after the different stowed period.

parameters for the CBT simulation were as follows: rigid specimen grip length l = 25.4 mm, initial grip angle Θ = 0.0712rad, specimen width w = 25.4 mm, gauge length s = 27.432 mm, laminate thickness t = 0.276 mm, and total fixture displacement δ = 25.4 mm. The composite laminate tested was composed of the plain woven M30S/PMT-F7 lamina with the $[\pm 45°]_4$ layup configuration, and the laminate directions 1, 2, and n are illustrated in Fig. 11(b). In the finite element simulation, the mechanical behavior of the single-ply lamina was characterized using a user-defined material subroutine (UMAT) that implements the present composite viscoelastic–viscoplastic model. The laminate shell behavior was defined by the ABAQUS built-in function "composite layup", based on classical laminate theory (CLT). The stress–strain response of each single-ply lamina was integrated into the shell mechanical response at each incremental step. The material parameters for the woven lamina are detailed in Table A.3 in Appendix. The viscoplastic component of the constitutive model was calibrated using available test data from a similar composite system, compensating for the lack of off-axis test data specific to the composite system used in the CBT validation.

5.2. Results and analysis

Fig. 12(c) shows the normalized moment–time curve of the composite laminate during the stowed period. The moment response $M(t)$ in the CBT is calculated using the following equation:

$$M(t) = P(t)D \tag{54}$$

where $P(t)$ represents the reaction force in the Y-direction at the fixture, and D denotes the offset distance by which the edge of the laminate deviates from the loading axis in the Z-direction. We note that under displacement-controlled loading, D remains constant, while the reaction force $P(t)$ decreases over time. This consequently results in a decrease in the reaction moment $M(t)$. To efficiently demonstrate the extent of reduction in the reaction moment over time, we normalized the reaction moment $M(t)$ by its instantaneous value M_0 and plotted the normalized moment $M(t)/M_0$ as a function of time in Fig. 12(c). Experimental data from Salazar and Fernandez (2021) are also plotted in the same figure for comparison. It is shown that in the initial time range, the moment decreases rapidly and then gradually slows in its rate of relaxation. Initially, the simulation aligns well with the experimental data, while at later times, a slight deviation appears, potentially due to the fitting error in the material model. Despite this, the model effectively captures the moment relaxation behavior observed in the composite laminate. Figs. 12(a) and 12(b) display the curvature-time curves of the composite laminate during the deployment and recovery periods. The curvature response $\kappa(t)$ in the CBT is calculated by:

$$\kappa(t) = \frac{\varphi(t)}{s} \tag{55}$$

where $\varphi(t)$ is the change in the rotation angle around the X-axis and s is the gauge length. The purple dash line in these figures represents the experimentally observed curvature history of the laminate during these periods. A residual curvature is evident in the laminate following the deployment period; part of this residual curvature is recoverable

during the recovery period, while the other part is permanent, indicating the formation of an irrecoverable residual curvature. Previous work by Long et al. (2022a) simulated curvature recovery in the CBT using a viscoelastic shell model, as illustrated by the blue dash line in Figs. 12(a) and 12(b). However, this model predicts that the residual curvature approaches zero during the recovery period, failing to capture the permanent curvature observed experimentally. In contrast, the numerical simulation of the CBT based on the present composite viscoelastic–viscoplastic constitutive model provides a better description of the time-dependent mechanical response of the laminate during the deployment and recovery periods. This model successfully captures both the curvature recovery and the permanent residual curvature, as shown by the red line in Figs. 12(a) and 12(b). It should be noted that, due to the absence of off-axis mechanical tests for M30S/PMT-F7 composites in the CBT, while the viscoelastic parameters for M30S/PMT-F7 are provided in Hamillage et al. (2024), the viscoplastic parameters were instead adopted from those of T300/Epoxy2500 in Kawai and Taniguchi (2006), as calibrated in Appendix. This approach resulted in an overestimation of the permanent residual deformation. Despite this limitation, the results demonstrate the capability of the proposed method to qualitatively capture the permanent deformation behavior of thin-walled composite laminates, thereby extending the simulation capabilities for composite deployable structures at both the material and structural levels. Additional CBT numerical simulations were conducted under consistent conditions, varying only the storage time of the composite laminate during the stowed period 0 hours, 2 hours, 4 hours, 30 days, and 365 days, respectively). Fig. 12(d) illustrates the curvature history during the deployment and recovery periods after different storage times. The results indicate that as storage time increases, both the residual curvature after the deployment period and the permanent residual curvature after recovery accumulate. These results suggest that variations in the storage time of composite deployable structures significantly impact their deployment and shape recovery behavior.

The CBT numerical simulations were performed repeatedly under consistent conditions, with the only variation being the layup of the composite laminate, which was modified to $[\pm0°]_4$, $[\pm15°]_4$, $[\pm30°]$, $[\pm35°]_4$ and $[\pm40°]_4$, respectively. Fig. 13(a) presents the curvature history of the composite laminate for different ply-angle layup configurations during the deployment and recovery periods. After the recovery period, the $[\pm45°]_4$ layup exhibited the largest residual curvature, whereas the $[\pm0°]_4$ layup showed the smallest residual curvature. This difference is attributed to the unique anisotropic mechanical behavior of woven composite laminate. The bending deformation response along the material direction of the composite laminate is governed by the stress–strain response of the individual plies, as described by classical laminate theory. For the $[\pm0°]_4$ layup, the primary stress–strain response in each single-ply lamina is oriented along the warp or weft direction, where the stress does not induce yield flow. Consequently, the accumulated plastic strain is minimal, resulting in the smallest permanent residual curvature. In contrast, for the $[\pm45°]_4$ layup, the primary stress–strain response is oriented in the shear direction, leading to the most significant yield effect and the largest accumulated plastic strain, which in turn results in the greatest permanent residual curvature. A larger permanent residual curvature after the recovery period indicates a greater deviation of the composite deployable structure from its designed configuration in service, thereby reducing service accuracy. The residual curvature of the composite laminate after the recovery period for different layup configurations is illustrated in Fig. 13(b) (yellow column). From a service accuracy perspective, the $[\pm0°]_4$ layup is the optimal configuration, while the $[\pm45°]_4$ layup is the least favorable. The maximum section bending moment of the composite laminate under different layups during the CBT loading history is shown in Fig. 13(b) (blue column). The smaller section moment observed for the $[\pm45°]_4$ layup, compared to the $[\pm0°]_4$ layup, is due to the lower stiffness of the plain woven lamina when the off-axis angle is 45°. The perspective of avoiding failure presents a different conclusion, the $[\pm0°]_4$ layup is the least favorable, while the $[\pm45°]_4$ layup is the most favorable, which explains why $[\pm45°]_4$ ply laminates are commonly used in the main bending direction in conventional designs of composite deployable structures, such as composite thin-ply lenticular tube booms (Salazar and Fernandez, 2021). In summary, the present constitutive model significantly enhances the simulation of permanent residual curvature in high-strain composite materials, thereby expanding the optimization design space for composite deployable structures. It offers a new design perspective and tool for improving deployment accuracy via minimizing permanent residual deformation without compromising the integrity of the composites. We would like to note that the proposed model is indeed a constitutive model for composite lamina. By implementing this model into the commercial finite element software ABAQUS through UMAT, and leveraging ABAQUS's robust pre- and post-processing capabilities, this approach is not limited by composite layup, structural design, or loading conditions, thereby demonstrating general feasibility. It is suitable not only for simulating CBT experiments but also for enhancing the simulation of other composite deployable structures, such as tape springs, storable tubular extendible members (STEM), and composite thin-walled lenticular tubes (CTLT).

6. Conclusions

An anisotropic viscoelastic–viscoplastic continuum constitutive model for composite laminates is developed to comprehensively describe the time-dependent mechanical behavior of high-strain composites used in advanced space deployable structures during folding, storage, unfolding, and recovery periods. The model integrates the viscoelastic equation in the form of the Boltzmann hereditary integral with anisotropic viscoplastic equations, incorporating assumptions in the yield function to avoid redundant parameters while effectively capturing the anisotropic mechanical behavior of the composites. This model characterizes the time-dependent off-axis mechanical behavior of both unidirectional and woven composite laminates, including rate-dependent stress–strain responses and creep behavior under constant stress. Notably, compared to the previous elastic–viscoplastic model of the composite lamina (Kawai and Masuko, 2004; Masuko and Kawai, 2004), the proposed model can also capture the hysteresis loop phenomenon in non-monotonic loading.

Furthermore, a significant contribution of this work lies in the proposed numerical implementation scheme. A two-step numerical solution strategy based on the return mapping algorithm, consisting of the "viscoelastic predictor" and the "viscoplastic corrector", is detailed. Originally proposed by Miled et al. (2011) for implementing an isotropic viscoelastic–viscoplastic constitutive model for polymers, this study extends the approach to the anisotropic case to effectively model composite lamina. The key of the numerical scheme is the derivation of the stress update algorithm for the viscoelastic model in full strain increment form, alongside a compact and general form of the return algorithm. These are implemented in a user-defined material subroutine (UMAT) within the commercial finite element code ABAQUS.

Finite element simulations of column bending tests on woven composite laminates, replicating the service conditions of real-world deployable structures, were conducted using the constitutive model developed in this paper. The FE model successfully captures the moment relaxation of the laminates during the storage period and the residual curvature recovery behavior during the recovery period in the column bending test. Notably, it is the first to capture the permanent residual curvature during recovery, an advancement over previous work (Long et al., 2022a). Additionally, the effects of storage time and layup schemes on the time-dependent mechanical responses of composite laminates during deployment and recovery periods were analyzed and discussed, highlighting the enhanced simulation capabilities of the developed constitutive model. The results indicate that longer storage times result in larger residual curvature. In conventional designs, a

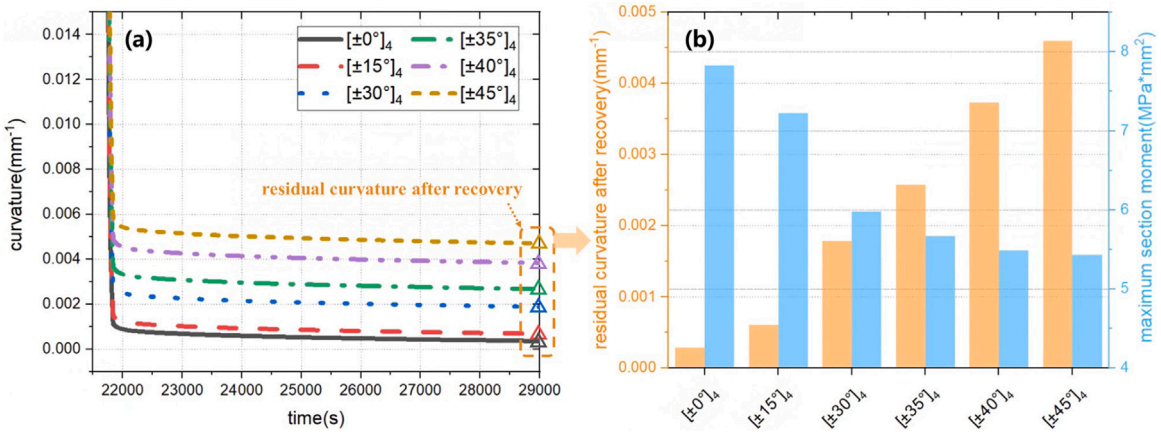

Fig. 13. Laminates mechanical responses at different angle-ply: (**a**) curvature-time curves of laminates during recovery at different angle-ply, (**b**) laminates residual curvature after 2.7 h recovery (yellow) and maximum section moment during stowed (blue) for different angle-ply.

$[\pm 45°]_4$ layup is typically employed in the main bending direction of deployable structures to minimize stress and avoid failure. However, the $[\pm 45°]_4$ layup exhibits the poorest shape recovery response of the composite laminate after deployment. These findings suggest that the model and simulation capabilities developed in this study offer a novel design perspective and tool for improving the deployment accuracy of composite deployable structures. Specifically, they provide insights into how to reduce permanent residual deformation and enhance deployment accuracy without compromising the structural integrity of the composites.

The limitations of this work must be acknowledged. To further enhance the calibration of the constitutive model, additional off-axis mechanical experiments on single-ply composite lamina are necessary. Moreover, a more focused investigation into the approach to obtaining decoupled material parameters of the composite viscoelastic–viscoplastic constitutive model from the experiments of time-dependent mechanical behavior should be pursued in future research. The model simulation capability could also be improved by considering the tension–compression asymmetry in the yield behavior of composites. Additionally, in present non-monotonic loading simulations, the predicted hysteresis loop phenomenon could not be quantitatively compared with experimental observations, this discrepancy may be attributed to the kinematic hardening behavior in real-world composites. Despite these areas for improvement, the present work provides a modeling framework capable of describing the time-dependent mechanical behavior of high-strain composites for deployable structures throughout the entire service life.

CRediT authorship contribution statement

Xiaowei Yue: Writing – review & editing, Writing – original draft, Visualization, Validation, Software, Methodology, Investigation, Funding acquisition, Formal analysis, Data curation, Conceptualization. **Ruiwen Guo:** Writing – review & editing, Visualization, Software, Investigation. **Ning An:** Writing – review & editing, Writing – original draft, Visualization, Supervision, Resources, Project administration, Funding acquisition, Formal analysis. **Jinxiong Zhou:** Writing – review & editing, Supervision, Resources, Project administration, Funding acquisition, Conceptualization.

Declaration of competing interest

The authors declare that they have no known competing financial interests or personal relationships that could have appeared to influence the work reported in this paper.

Acknowledgments

This research is supported by the National Natural Science Foundation of China (grant 11972277 and 12202295), by the Fundamental Research Funds for the Central Universities (grant xzy022024052 and YJ2021137), and by the Natural Science Foundation of Sichuan Province (grant 25QNJJ4363).

Appendix. Calibration of material parameters

Since the total strain in the constitutive model developed in the main text is decomposed into a viscoelastic part and a viscoplastic part, in this section, we separately calibrate the parameters for each part.

I. Calibration of viscoelastic properties: For modeling a single-ply thin lamina as a homogenized orthotropic viscoelastic plate, as outlined in Kaw (2005), An et al. (2022), Kwok and Pellegrino (2017), the stress–strain relationship for the lamina can be described by a reduced relaxation stiffness matrix, $\mathbf{Q}(t)$, as follows:

$$\boldsymbol{\sigma}(t) = \mathbf{Q}(t)\boldsymbol{\epsilon}(t) \tag{A.1}$$

where $\boldsymbol{\sigma}(t)$ and $\boldsymbol{\epsilon}(t)$ represent the in-plane stress and strain vectors of the lamina, respectively. The reduced relaxation stiffness matrix, $\mathbf{Q}(t)$, is given by:

$$\mathbf{Q}(t) = \begin{bmatrix} Q_{11}(t) & Q_{12}(t) & 0 \\ Q_{12}(t) & Q_{22}(t) & 0 \\ 0 & 0 & Q_{66}(t) \end{bmatrix} \tag{A.2}$$

where the components $Q_{11}(t)$, $Q_{12}(t)$, $Q_{22}(t)$, and $Q_{66}(t)$ are time-dependent and capture the viscoelastic nature of the lamina, expressed in the form of a Prony series as follows:

$$Q_{ij}(t) = Q_{ij,0}\left(1 - \sum_{k=1}^{n} q_k \left(1 - e^{-t/\rho_k}\right)\right) \tag{A.3}$$

where $Q_{ij,0}$ represents the instantaneous stiffness matrix of the composite lamina, n denotes the number of terms in the Prony series, $q_k = \frac{Q_{ij,k}}{Q_{ij,0}}$ represents the relative stiffness in the $k-$th term, indicating the fraction of $Q_{ij,0}$ that relaxes with a characteristic relaxation time ρ_k. After long-term relaxation, the equilibrium stiffness coefficient $Q_{ij,\infty} = Q_{ij,0} - \sum_{k=1}^{N} Q_{ij,k}$ represents the stiffness that remains after all relaxation has taken place.

Finally, we note that to calibrate the constants in Eq. (A.3), the instantaneous stiffness coefficient $Q_{ij,0}$ can be readily determined from the engineering constants of the lamina. The expression is given as follows.

$$Q_{11,0} = \frac{E_1}{1 - \upsilon_{21}\upsilon_{12}}, Q_{12,0} = \frac{\upsilon_{12}E_2}{1 - \upsilon_{21}\upsilon_{12}}, Q_{22,0} = \frac{E_2}{1 - \upsilon_{21}\upsilon_{12}}, \text{ and } Q_{66,0} = G_{12} \tag{A.4}$$

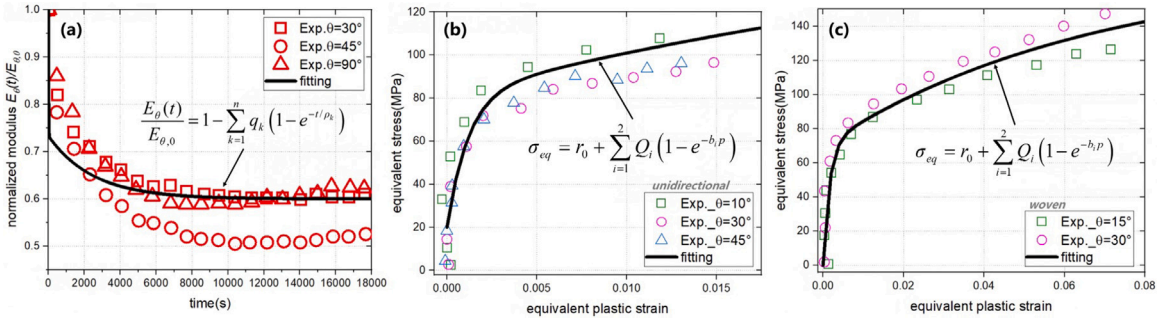

Fig. A1. Example of constitutive model parameter fitting: (**a**) fitting relaxation data based on Prony's series, (**b**) fitting equivalent stress-equivalent plastic strain data of unidirectional lamina based on hardening function, (**c**) fitting equivalent stress-equivalent plastic strain data of woven lamina based on hardening function.

Meanwhile, the other parameters, such as n, q_k, and ρ_k, can be obtained through relaxation tests and fitting procedures.

In Section 4 of the main text, we noted that a unidirectional lamina and a single-ply woven lamina were employed for validation. Here, we provide the calibration of their material properties.

Specifically, the unidirectional lamina, referred to as T800H/Epoxy3631, was calibrated using experimental data from Masuko and Kawai (2004). First, the engineering constants provided were used to calculate $Q_{ij,0}$ through Eq. (A.4). Next, the Prony series parameters were fitted using three off-axis relaxation tests at angles of $\theta = 30°$, 45°, and 90°. The relaxation modulus of the lamina for these off-axis responses was normalized with the instantaneous modulus as follows:

$$\frac{E_\theta(t)}{E_{\theta,0}} = 1 - \sum_{k=1}^{n} q_k \left(1 - e^{-t/\rho_k}\right) \tag{A.5}$$

The fitting, as shown in Fig. A1(a), resulted in a two-term Prony series with $n = 2$, $q_1 = 0.266$, $q_2 = 0.133$, $\rho_1 = 10$, and $\rho_2 = 2500$. With these parameters substituted into Eq. (A.3), the viscoelastic properties of the unidirectional lamina T800H/3631 were determined and are listed in Table A.1.

On the other hand, the single-ply woven lamina, T300/Epoxy2500, was calibrated using experimental data from Kawai and Taniguchi (2006). The woven lamina is assumed to behave as an elastic–viscoplastic material; therefore, Q_{ij} is time-independent. Only the engineering constants were used for calibration with Eq. (A.4), and the results are provided in Table A.2.

II. Calibration of viscoplastic properties: The parameters for the viscoplastic components of the constitutive model are calibrated using off-axis tensile test data from the single-ply composite lamina. A crucial step in this process involves deriving the equivalent stress-equivalent plastic strain master curve from the off-axis stress–strain response, based on the assumptions regarding the yield and plastic flow behavior of unidirectional and woven lamina made in Sun and Chen (1989). This master curve is then used for parameter fitting.

The off-axis tensile stress can be transformed to the local material coordinate system as follows:

$$\sigma_{11} = \sigma_x \cos^2\theta \tag{A.6}$$

$$\sigma_{22} = \sigma_x \sin^2\theta \tag{A.7}$$

$$\sigma_{12} = -\sigma_x \cos\theta \sin\theta \tag{A.8}$$

where θ is the off-axis angle, σ_x represents the axial stress response, and σ_{ij} denotes the stress components in the material coordinate system. Then, the equivalent stress for the unidirectional and woven composite lamina can be obtained by substituting Eq. (A.6), (A.7), and (A.8) into Eqs. (13) and (16) in the main text, respectively:

$$\sigma_{eq}^{UD} = \sigma_x \sqrt{\frac{3}{2}\left(\sin^4\theta + 2a_{66}\sin^2\theta\cos^2\theta\right)} \tag{A.9}$$

and

$$\sigma_{eq}^{W} = \sigma_x \sqrt{3}\sin\theta\cos\theta \tag{A.10}$$

The above equations can be written as:

$$\sigma_{eq} = \sigma_x h(\theta) \tag{A.11}$$

where $h(\theta)$ is the orientation factor, which has different expressions for unidirectional and woven composites. The corresponding equivalent plastic strain p is:

$$p = \frac{\epsilon_x^p}{h(\theta)} \tag{A.12}$$

where

$$\epsilon_x^p = \epsilon_x - \frac{\sigma_x}{E_x} \tag{A.13}$$

where ϵ_x represents the axial strain.

The off-axis tension test stress–strain data for the unidirectional and woven lamina were sourced from the literature (Kawai and Masuko, 2004; Kawai and Taniguchi, 2006), respectively. Specifically, for the unidirectional lamina T800H/Epoxy3631, three sets of off-axis tension stress–strain data were collected for calibration, with $\theta = 10°$, 30°, and 45°. For the woven composite lamina T300/Epoxy2500, two sets of off-axis tension stress–strain data were collected for calibration, with $\theta = 15°$ and 30°. These off-axis stress–strain data were converted to equivalent stress–equivalent plastic strain master curves using Eq. (A.6)–(A.13), as illustrated in Figs. A1(b) and A1(c). The master curves were then utilized to fit the viscoplastic material parameters based on the hardening law discussed in Section 2.

For the unidirectional lamina, the anisotropy coefficient a_{66} is determined by obtaining the master curve with the least dispersion, resulting in $a_{66} = 1.3$. The detailed process for determining the viscosity equation parameters K and m can be found in Kawai and Masuko (2004). To simplify model calibration, the material parameter $K = 1$ MPa s^m is set in the viscosity equation to maintain the overstress σ_v at a low level. Consequently, the time-dependent mechanical response in the model is primarily described by the relaxation moduli. The fitted viscoplastic parameters are listed in Table A.1 for the unidirectional lamina. In addition, an E–VP model was also fitted for the unidirectional lamina for comparison, and the resulting parameters are: $a_{66} = 1.3$, $r_0 = 17$ MPa, $b_1 = 900$, $b_2 = 45$, $Q_1 = 28$ MPa, $Q_2 = 70$ MPa, $K = 150$ MPa s^m, and $m = 0.205$. Similarly, the viscoplastic parameters for the woven composite lamina T300/Epoxy2500 were obtained and are listed in Table A.2.

Data availability

The raw/processed data required to reproduce these findings are available to download from https://github.com/XJTU-Zhou-group/ABAQUS_UMAT_HSCcompVEVP.

Table A.1
VE–VP model parameters for unidirectional T800H/Epoxy3631 lamina.

viscoelastic						reference
i	ρ_i (s)	$Q_{11,i}$ (MPa)	$Q_{12,i}$ (MPa)	$Q_{22,i}$ (MPa)	$Q_{66,i}$ (MPa)	
∞		104 000	1776	5004	2106	fit (Masuko and Kawai, 2004)
1	10	46 133	789	2224	936	fit (Masuko and Kawai, 2004)
2	2500	23 067	395	1112	468	fit (Masuko and Kawai, 2004)
viscoplastic						
hardening laws:	$b_1 = 844$		$Q_1 = 62$ MPa			fit (Kawai and Masuko, 2004)
	$b_2 = 22$		$Q_2 = 96$ MPa			fit (Kawai and Masuko, 2004)
	$r_0 = 20$ MPa					defined
viscosity equation:	$K = 1$ (MPa s)^m		$m = 0.205$			defined
anisotropy coefficient:	$a_{66} = 1.3$					Kawai and Masuko (2004)

Table A.2
E–VP model parameters for woven T300/Epoxy2500 lamina.

elastic						reference
i	ρ_i (s)	$Q_{11,i}$ (MPa)	$Q_{12,i}$ (MPa)	$Q_{22,i}$ (MPa)	$Q_{66,i}$ (MPa)	
0		54 205	1410.5	54 205	3800	Kawai and Taniguchi (2006)
viscoplastic						
hardening laws:	$b_1 = 643$		$Q_1 = 70$ MPa			fit (Kawai and Taniguchi, 2006)
	$b_2 = 15$		$Q_2 = 104$ MPa			fit (Kawai and Taniguchi, 2006)
	$r_0 = 0$ MPa					fit (Kawai and Taniguchi, 2006)
viscosity equation:	$K = 1$ (MPa s)^m		$m = 0.205$			defined

Table A.3
VE–VP model parameters of woven lamina M30S/PMT-F7 for CBT.

viscoelastic						reference
i	ρ_i (s)	$C_{11,i}$ (MPa)	$C_{12,i}$ (MPa)	$C_{22,i}$ (MPa)	$C_{33,i}$ (MPa)	
∞		60 577.95	15 823.53	60 577.95	2916.38	Hamillage et al. (2024)
1	0.9563	410.595	11.595	410.595	113.405	Hamillage et al. (2024)
2	9.697	281.005	7.025	281.005	76.945	Hamillage et al. (2024)
3	93.78	11.52	395	588.16	157.78	Hamillage et al. (2024)
4	981.1	176.385	2.865	176.385	46.845	Hamillage et al. (2024)
5	9283	660.28	8.7	660.28	173.16	Hamillage et al. (2024)
6	97 210	291.2	0.22	291.2	72.8	Hamillage et al. (2024)
7	963 100	259.325	3.885	259.325	68.855	Hamillage et al. (2024)
8	9 472 000	683.185	4.095	683.185	164.115	Hamillage et al. (2024)
9	56 310 000	272.925	3.075	272.925	75.025	Hamillage et al. (2024)
viscoplastic						
hardening laws:	$b_1 = 643$		$Q_1 = 70$ MPa			fit (Kawai and Taniguchi, 2006)
	$b_2 = 15$		$Q_2 = 104$ MPa			fit (Kawai and Taniguchi, 2006)
	$r_0 = 0$ MPa					fit (Kawai and Taniguchi, 2006)
viscosity equation:	$K = 1$ (MPa s)^m		$m = 0.205$			defined

References

An, N., Jia, Q., Jin, H., Ma, X., Zhou, J., 2022. Multiscale modeling of viscoelastic behavior of unidirectional composite laminates and deployable structures. Mater. Des. 219, 110754.

Bai, J.-B., You, F.-Y., Wang, Z.-Z., Fantuzzi, N., Liu, Q., Xi, H.-T., Bu, G.-Y., Wang, Y.-B., Wu, S.-Q., Feng, R., et al., 2024. An efficient multi-objective optimization framework for thin-walled tubular deployable composite boom. Compos. Struct. 327, 117713.

Borowski, E.C., Soliman, E.M., Khan, A.I., Taha, M.M.R., 2018. Stowage and deployment of a viscoelastic orthotropic carbon-fiber composite tape spring. J. Spacecr. Rockets 55 (4), 829–840.

Brinkmeyer, A., Pellegrino, S., Weaver, P.M., 2016. Effects of long-term stowage on the deployment of bistable tape springs. J. Appl. Mech. 83 (1), 011008.

Caruso, M.M., Davis, D.A., Shen, Q., Odom, S.A., Sottos, N.R., White, S.R., Moore, J.S., 2009. Mechanically-induced chemical changes in polymeric materials. Chem. Rev. 109 (11), 5755–5798.

Chaboche, J.-L., 2008. A review of some plasticity and viscoplasticity constitutive theories. Int. J. Plast. 24 (10), 1642–1693.

Chen, Y., Nan, T., Yun, G.J., Zhang, C., 2022. Micromechanical modeling of the viscoelastic–viscoplastic response of fiber-reinforced composites. Internat. J. Engrg. Sci. 181, 103767.

Cho, J., Fenner, J., Werner, B., Daniel, I., 2010. A constitutive model for fiber-reinforced polymer composites. J. Compos. Mater. 44 (26), 3133–3150.

Coenen, E., Kouznetsova, V., Geers, M., 2012. Multi-scale continuous–discontinuous framework for computational-homogenization–localization. J. Mech. Phys. Solids 60 (8), 1486–1507.

Dassault, S., 2014. Abaqus 6.14 documentation. Simulia Syst. Providence, RI, USA.

Deng, J., An, N., Jia, Q., Ma, X., 2024. Deployment analysis of composite thin-walled lenticular tubes with effect of storage time and temperature. Chin. J. Aeronaut. 37 (1), 162–172.

Fallahi, H., Taheri-Behrooz, F., Asadi, A., 2020. Nonlinear mechanical response of polymer matrix composites: a review. Polymer Rev. 60 (1), 42–85.

Fernandes, P., Sousa, B., Marques, R., Tavares, J.M.R., Marques, A., Jorge, R.N., Pinto, R., Correia, N., 2021. Influence of relaxation on the deployment behaviour of a cfrp composite elastic–hinge. Compos. Struct. 259, 113217.

Fernandez, J.M., Murphey, T.W., 2018. A simple test method for large deformation bending of thin high strain composite flexures. In: 2018 AIAA Spacecraft Structures Conference. p. 0942.

Ferraro, S., Pellegrino, S., 2021. Topology and shape optimization of ultrathin composite self-deployable shell structures with cutouts. AIAA J. 59 (9), 3696–3709.

Feyel, F., Chaboche, J.-L., 2000. FE2 multiscale approach for modelling the elasto-viscoplastic behaviour of long fibre SiC/Ti composite materials. Comput. Methods Appl. Mech. Engrg. 183 (3–4), 309–330.

Firth, J.A., Pankow, M.R., 2020. Minimal unpowered strain-energy deployment mechanism for rollable spacecraft booms: ground test. J. Spacecr. Rockets 57 (2), 346–353.

Frank, G.J., Brockman, R.A., 2001. A viscoelastic–viscoplastic constitutive model for glassy polymers. Int. J. Solids Struct. 38 (30–31), 5149–5164.

Ghosh, S., Lee, K., Moorthy, S., 1995. Multiple scale analysis of heterogeneous elastic structures using homogenization theory and voronoi cell finite element method. Int. J. Solids Struct. 32 (1), 27–62.

Goda, I., Assidi, M., Ganghoffer, J.-F., 2013. Equivalent mechanical properties of textile monolayers from discrete asymptotic homogenization. J. Mech. Phys. Solids 61 (12), 2537–2565.

Guo, R., Jin, X., Jia, Q., Ma, X., An, N., Zhou, J., 2023. Folding, stowage, and deployment of composite thin-walled lenticular tubes. Acta Astronaut. 213, 567–577.
Hahn, H.T., Tsai, S.W., 1973. Nonlinear elastic behavior of unidirectional composite laminae. J. Compos. Mater. 7 (1), 102–118.
Hamillage, M.Y., Klimm, W., Kwok, K., Fernandez, J.M., 2024. Shape recovery simulation of viscoelastic thin-ply composite coilable booms. Acta Astronaut. 215, 607–617.
Hamillage, M.Y., Leung, C., Kwok, K., 2022. Viscoelastic modeling and characterization of thin-ply composite laminates. Compos. Struct. 280, 114901.
Hill, R., 1998. The mathematical theory of plasticity, vol. 11, Oxford University Press.
Jäger, J., Sause, M.G., Burkert, F., Moosburger-Will, J., Greisel, M., Horn, S., 2015. Influence of plastic deformation on single-fiber push-out tests of carbon fiber reinforced epoxy resin. Composites A 71, 157–167.
Jia, Q., An, N., Ma, X., Zhou, J., 2021. Exploring the design space for nonlinear buckling of composite thin-walled lenticular tubes under pure bending. Int. J. Mech. Sci. 207, 106661.
Jin, H., An, N., Jia, Q., Ma, X., Zhou, J., 2024. A mesoscale computational approach to predict ABD matrix of thin woven composites. Compos. Struct. 337, 118031.
Jin, H., Jia, Q., An, N., Zhao, G., Ma, X., Zhou, J., 2022. Surrogate modeling accelerated shape optimization of deployable composite tape-spring hinges. AIAA J. 60 (10), 5942–5953.
Kaw, A.K., 2005. Mechanics of composite materials. CRC Press.
Kawai, M., Masuko, Y., 2004. Creep behavior of unidirectional and angle-ply T800H/3631 laminates at high temperature and simulations using a phenomenological viscoplasticity model. Compos. Sci. Technol. 64 (15), 2373–2384.
Kawai, M., Masuko, Y., Kazama, T., Nakao, T., 2020. Off-axis stress relaxation behavior of unidirectional T800H/epoxy at elevated temperature and its macromechanical analysis. In: Durability Analysis of Composite Systems 2001. CRC Press, pp. 369–374.
Kawai, M., Taniguchi, T., 2006. Off-axis fatigue behavior of plain weave carbon/epoxy fabric laminates at room and high temperatures and its mechanical modeling. Composites A 37 (2), 243–256.
Kim, S.J., Cho, J.Y., 1992. Role of matrix in viscoplastic behavior of thermoplastic composites at elevated temperature. AIAA J. 30 (10), 2571–2573.
Klimm, W., Kwok, K., 2020. Surface accuracy of viscoelastic composite thin-shell deployable reflector antennas. In: AIAA Scitech 2020 Forum. p. 0932.
Kwok, K., Pellegrino, S., 2013. Folding, stowage, and deployment of viscoelastic tape springs. AIAA J. 51 (8), 1908–1918.
Kwok, K., Pellegrino, S., 2017. Micromechanics models for viscoelastic plain-weave composite tape springs. AIAA J. 55 (1), 309–321.
Liu, T.-W., Bai, J.-B., Fantuzzi, N., Bu, G.-Y., Li, D., 2022. Multi-objective optimisation designs for thin-walled deployable composite hinges using surrogate models and genetic algorithms. Compos. Struct. 280, 114757.
Liu, T.-W., Bai, J.-B., Fantuzzi, N., Zhang, X., 2024. Thin-walled deployable composite structures: A review. Prog. Aerosp. Sci. 146, 100985.
Liu, X., Rouf, K., Peng, B., Yu, W., 2017. Two-step homogenization of textile composites using mechanics of structure genome. Compos. Struct. 171, 252–262.
Liu, X., Tang, T., Yu, W., Pipes, R.B., 2018. Multiscale modeling of viscoelastic behaviors of textile composites. Internat. J. Engrg. Sci. 130, 175–186.
Long, Y., Rique, O., Fernandez, J.M., Bergan, A.C., Salazar, J.E., Yu, W., 2022a. Simulation of the column bending test using an anisotropic viscoelastic shell model. Compos. Struct. 288, 115376.
Long, Y., Yu, W., Fernandez, J.M., Bergan, A., 2022b. Mechanics of structure genome-based nonlinear shell analysis. In: AIAA SciTech 2022 Forum. p. 1119.
Ma, X., An, N., Cong, Q., Bai, J.-B., Wu, M., Xu, Y., Zhou, J., Zhang, D., Zhang, T., Guo, R., et al., 2024. Design, modeling, and manufacturing of high strain composites for space deployable structures. Commun. Eng. 3 (1), 78.
Ma, X., Li, T., Ma, J., Wang, Z., Shi, C., Zheng, S., Cui, Q., Li, X., Liu, F., Guo, H., et al., 2022. Recent advances in space-deployable structures in China. Engineering 17, 207–219.
Mao, H., Shipsha, A., Tibert, G., 2017. Design and analysis of laminates for self-deployment of viscoelastic bistable tape springs after long-term stowage. J. Appl. Mech. 84 (7), 071004.
Masuko, Y., Kawai, M., 2004. Application of a phenomenological viscoplasticity model to the stress relaxation behavior of unidirectional and angle-ply CFRP laminates at high temperature. Composites A 35 (7–8), 817–826.
Miled, B., Doghri, I., Delannay, L., 2011. Coupled viscoelastic–viscoplastic modeling of homogeneous and isotropic polymers: Numerical algorithm and analytical solutions. Comput. Methods Appl. Mech. Engrg. 200 (47–48), 3381–3394.
Murphey, T.W., Francis, W., Davis, B., Mejia-Ariza, J.M., 2015. High strain composites. In: 2nd AIAA Spacecraft Structures Conference. p. 0942.
Nikolov, S., Doghri, I., Pierard, O., Zealouk, L., Goldberg, A., 2002. Multi-scale constitutive modeling of the small deformations of semi-crystalline polymers. J. Mech. Phys. Solids 50 (11), 2275–2302.
Noh, J., Whitcomb, J., 2003. Efficient techniques for predicting viscoelastic behavior of sublaminates. Composites B 34 (8), 727–736.
Odegard, G., Searles, K., Kumosa, M., 2000. Nonlinear analysis of woven fabric-reinforced graphite/PMR-15 composites under shear-dominated biaxial loads. Mech. Compos. Mater. Struct. 7 (2), 129–152.
Ogihara, S., Reifsnider, K.L., 2002. Characterization of nonlinear behavior in woven composite laminates. Appl. Compos. Mater. 9 (4), 249–263.
Omairey, S.L., Dunning, P.D., Sriramula, S., 2019. Development of an ABAQUS plugin tool for periodic RVE homogenisation. Eng. Comput. 35, 567–577.
Perzyna, P., 1966. Fundamental problems in viscoplasticity. Adv. Appl. Mech. 9, 243–377.
Rique, O., Liu, X., Yu, W., Pipes, R.B., 2020. Constitutive modeling for time-and temperature-dependent behavior of composites. Composites B 184, 107726.
Rouf, K., Liu, X., Yu, W., 2018. Multiscale structural analysis of textile composites using mechanics of structure genome. Int. J. Solids Struct. 136, 89–102.
Ryou, H., Chung, K., 2009. Development of viscoelastic/rate-sensitive-plastic constitutive law for fiber-reinforced composites and its applications part II: Numerical formulation and verification. Compos. Sci. Technol. 69 (2), 292–299.
Salazar, J.E., Fernandez, J.M., 2021. Experimental characterization of the dimensional stability of deployable composite booms during stowage. In: AIAA SciTech 2021 Forum. p. 0195.
Simo, J.C., Taylor, R.L., 1985. Consistent tangent operators for rate-independent elastoplasticity. Comput. Methods Appl. Mech. Engrg. 48 (1), 101–118.
Sun, C., Chen, J., 1989. A simple flow rule for characterizing nonlinear behavior of fiber composites. J. Compos. Mater. 23 (10), 1009–1020.
Sun, C., Gates, T., 1990. Elastic/visoplastic constitutive model for fiber reinforced thermoplastic composites. AIAA J. 29, 457–463.
Taylor, R.L., Pister, K.S., Goudreau, G.L., 1970. Thermomechanical analysis of viscoelastic solids. Internat. J. Numer. Methods Engrg. 2 (1), 45–59.
Ubamanyu, K., Ghedalia, D., Hasanyan, A.D., Pellegrino, S., 2020. Experimental study of time-dependent failure of high strain composites. In: AIAA Scitech 2020 Forum. p. 0207.
Voce, E., 1955. A practical strain hardening function. Metallurgia 51, 219–226.
Wang, B., Zhu, J., Zhong, S., Liang, W., Guan, C., 2023. Space deployable mechanics: A review of structures and smart driving. Mater. Des. 112557.
Yang, J., Yang, X., Zhu, H., Shi, D., Chen, X., Qi, H., 2018. The effect of off-axis angles on the mesoscale deformation response and failure behavior of an orthotropic textile carbon-epoxy composite. Compos. Struct. 206, 952–959.
Yapa Hamillage, M.M., Klimm, W.J., Kwok, K., 2022. Permanent shape change of thin-ply composites. In: AIAA Scitech 2022 Forum. p. 1117.
Yu, W., 2019. Simplified formulation of mechanics of structure genome. AIAA J. 57 (10), 4201–4209.
Yu, W., 2024. A review of modeling of composite structures. Materials 17 (2), 446.
Yue, X., Zhou, J., 2023. Implementation of ABAQUS user subroutines for viscoplasticity of 316 stainless steel and zircaloy-4. Metals 13 (9), 1554.
Zhang, L., Klimm, W.J., Kwok, K., Yu, W., 2022. A nonlinear viscoelastic-viscoplastic constitutive model for epoxy polymers. In: AIAA SciTech 2022 Forum. p. 1120.